EXPERIMENTAL OBSERVATION OF NEOCLASSICAL CURRENTS

by

Michael Charles Zarnstorff

A thesis submitted in partial fulfillment

of the requirements for the degree of

DOCTOR OF PHILOSOPHY

(Physics)

at the

University of Wisconsin-Madison

1984

EXPERIMENTAL OBSERVATION OF NEOCLASSICAL CURRENTS

Michael Charles Zarnstorff

Under the supervision of Associate Professor Stewart C. Prager

The parallel and perpendicular equilibrium currents have been experimentally studied in the Levitated Octupole, with toroidal field. Observations of the spatial structure, collisionality and toroidal field dependence of the complete current and the ion portion of the current are presented. Experimentally measured currents are compared to neoclassical current distributions calculated for the actual machine geometry. Measurements of the total plasma parallel current for absolute-MHD-stable flux surfaces (inside the separatrix) agree well with theory, showing the bootstrap and Pfirsch-Schlüter currents as predicted by neoclassical transport theory. On average-MHD-stable flux surfaces (outside the separatrix) there is more parallel current than predicted by theory, though the spatial structure is correct. Separate measurements of the ion parallel and perpendicular currents agree with theory, showing the lack of measurable ion poloidal rotation in all situations.

Acknowledgements

I would like to thank my advisor, Professor S.C. Prager, for his interest, support, and tolerance throughout my graduate research. I also thank Professor J.D. Callen for many insightful discussions and for providing enthusiasm and guidance on theoretical matters.

I am grateful to my initial advisor, Professor D.W. Kerst, and to Professor R.S. Post for their exemplary research styles and for much advice not always promptly appreciated.

This work is an outgrowth of previous high-β studies, during which I had the pleasure of collaborating with Dr. A.G. Kellman. S.V. Painchaud is my successor in this work, and has assisted in some of its later aspects. I would like to thank my officemate, Trudy D. Rempel, and the other graduate students for many interesting discussions, helpful ideas, and for reminding me of life outside physics.

This work would not have been possible without the efforts of J. Laufenberg and his "hourly" workers helping build and maintain the apparatus. In addition, I have had many profitable discussions with him, T. Loveil, and P. Nonn regarding the design of the diagnostics developed in the course of this work.

Finally, I would thank my wife, Sally, for her patience and understanding.

This research was supported by the U.S. Department of Energy.

Table of Contents

Chapter 1

Introduction

Neoclassical plasma transport theory[1,2] considers the flux of particles, energy, and electric charge (current) due to the interaction of Coulomb collisions, single particle drift across magnetic flux surfaces, and gradients of temperature or density. Neoclassical transport is to be distinguished from classical transport[3] which is due to the interaction of Coulomb collisions and the single particle gyration about the magnetic field in the presence of temperature and density gradients. Neoclassical transport theory predicts a full set of relations between certain thermodynamic forces and fluxes

$$\begin{bmatrix} \Gamma_\perp \\ Q_\perp \\ J_\parallel \end{bmatrix} = \begin{bmatrix} L_{11} & L_{12} & L_{13} \\ L_{21} & L_{22} & L_{23} \\ L_{31} & L_{32} & L_{33} \end{bmatrix} \begin{bmatrix} \nabla_\perp p \\ \nabla_\perp T \\ E_\parallel \end{bmatrix},$$

where $\Gamma_\perp$ and $Q_\perp$ are the flux of particles and heat across the flux surface, $J_\parallel$ is the current (flux of charge) parallel to the magnetic field, $\nabla_\perp p$ and $\nabla_\perp T$ are the cross-flux-surface gradients of kinetic pressure and temperature, and $E_\parallel$ is the electric field component parallel to the magnetic field. The diagonal transport coefficients, L_{jj}, relate similar forces and fluxes, and are the diffusion and heat conduction coefficients and the electrical conductivity. The off diagonal elements couple dissimilar forces and

fluxes, and by Onsager's Theorem are inter-related by various symmetry relations. The coefficients of particular interest in this thesis are L_{31} and L_{32}. These coefficients imply[4,5] that current should flow parallel to the magnetic field in a toroidal confinement system with helical magnetic fields, such as tokamaks, stellarators, and multipoles; and predicts related currents for non-axisymmetric tandem mirrors.[6] This parallel current is driven by a perpendicular pressure or temperature gradient, and consists of two superimposed parts: The Pfirsch-Schlüter current[7] maintains charge neutrality in the presence of the diamagnetic current, is independent of particle collision frequency, and has varying sign along a magnetic field line, but averages to zero. The bootstrap current[4,5] is generated by the balancing of electron-ion friction with the viscous stress between trapped and untrapped particles, increases with decreasing collision frequency, and is unidirectional along a magnetic field line. The fluid forces that act to determine these currents (fluid frictions and viscous forces) also determine the other flows. In a similar (kinetic) sense, all the neoclassical transport relations are determined by the same perturbed distribution function, thus these currents are an intrinsic part of neoclassical transport theory.

The practical potential of the bootstrap current for generating a steady-state tokamak and driving instabilities was quickly recognized.[5] Indeed, in an ignited tokamak reactor these currents would provide all the current necessary for the confining poloidal magnetic field, without

any additional Ohmic current. In addition, the L_{13} coefficient generates a cross-flux-surface flux of particle due to an applied $E_{\|}$ (the Ware pinch[8]). This pinch effect is often invoked in tokamak design studies to aid refueling of the central plasma. However, by Onsager symmetry the Ware pinch should only be expected in the presence of the neoclassical currents.

Previous attempts to experimentally identify either the Pfirsch-Schlüter or bootstrap currents in stellarators[9, 10, 11] and tokamaks[12] have been unsuccessful or inconclusive.

This thesis reports the first observation of these currents in a study performed on the Wisconsin Levitated Octupole. Careful measurements of the spatial structure, dependence on toroidal magnetic field strength (or field line pitch), and collisionality dependence of both the complete plasma current (electrons and ions) and the ion portion of the current are in good agreement with theory for most of the flux surfaces (the inner 3/4 of the stable flux). Current on flux surfaces that are near the outside of the plasma is found not to be in good agreement with theory, in that the parallel current is larger than expected. This work is an outgrowth of previous studies[13, 14] that studied high-β ($\beta \equiv$ plasma pressure/magnetic field pressure) plasmas in the same device.

The Octupole, and multipoles in general, are almost ideally suited for the study of equilibrium currents since: (1) The neoclassical current is not obscured by ohmic currents, as the magnetic field is dominantly established by currents in the boundary conductors. (2) Probes can be used

to measure local plasma parameters and currents, as there are no runaway electrons from an ohmic current. (3) Using Marshall gun injected plasmas, high pressure (and thus high pressure gradient) plasmas are easily generated.[14] (4) Plasma parameters and magnetic field strength and transform can be varied independently. (5) The parallel gradient scale length of the magnetic field is relatively short ($\sim$ 0.6 m) allowing access to the various collisionality regimes at moderate plasma parameters. (6) Neoclassical transport theory, as formulated for tokamaks, provides a prediction of the equilibrium currents for multipoles, and thus can be tested by this experiment.

This thesis consists of four parts: Chapter 2 describes the experimental device, plasma diagnostics including the diagnostics used to measure the currents, and experimentally measured parameters of the plasmas used in the study. Chapter 3 presents a physical explanation and summarizes the theory of neoclassical currents, using the recent moment equation approach.[15] It also presents calculations of the characteristics of the neoclassical currents for the actual Octupole geometry. Chapter 4 presents the experimental neoclassical current measurements, and compares them to the theoretical predictions. Measurements of both total and ion currents on several flux surfaces are discussed. Chapter 5 summarizes the work, and considers future research directions.

Chapter 2

Experimental Apparatus

In this chapter the experimental apparatus, diagnostics and method are discussed. Emphasis is placed on those aspects that are novel or peculiar to this work.

2.1. Machine Description

All of the experiments described here were conducted on the Wisconsin Levitated Octupole[16] Fig. 2-1. This device has been extensively described in the literature[17,18,19,20] so only a brief description is included here.

The Octupole is a toroidal aluminum vacuum vessel of approximately square cross section, containing four aluminum hoops. Physical dimensions, and other parameters are listed in Table 2-1. The vessel has poloidal and toroidal electrical breaks for the introduction of poloidal and toroidal magnetic fields. The toroidal magnetic field is generated by directly driving currents in the vacuum vessel. The poloidal magnetic field is generated by exciting an iron core (threading the toroid) which inductively drives boundary currents in the four hoops and in the vacuum vessel. Continuity windings connect opposite sides of the poloidal break providing, for the vessel boundary currents, an electrically short path

Table 2-1

Octupole Parameters

Major radius	1.4 m
Minor cross section	1.12 m x 1.2 m
Hoop minor-radius	8.89 cm
Vacuum volume	8.6 m^3
Stable plasma volume	7.7 m^3
Base pressure	5 x 10^{-9} torr
Half-sine magnetic field period	43 msec
Crowbarred decay time	70 msec
Peak poloidal field core flux	0.72 Wb
Total poloidal field energy	0.6 MJ
Maximum toroidal field (at axis)	~600 G

around the break, and allowing control of the distribution of the boundary currents at the break. Ideally, these continuity windings are arranged to ensure that the boundary current distribution and poloidal magnetic field are axisymmetric within the vessel.

The calculated[21,22] resulting poloidal magnetic flux plot is shown in Fig. 2-2. All flux surfaces are referred to by a number between 0 and 10, giving the amount of poloidal flux contained in the surface in units of $1/10^{ths}$ of the peak (during the pulse) machine flux. Thus, the flux

surface labeled 0 is in the hoops, and the flux surface labeled 10 is in the vessel wall at peak field. The flux surfaces are divided into three regions: Flux surfaces within the separatrix, $\psi_{Sep} \simeq 5.7$, are entirely of good curvature, and are absolute-MHD-stable. Flux surfaces between the separatrix and $\psi_{Crit} \simeq 8.2$ are average-MHD-stable, containing regions of good and bad curvature. Flux surfaces ouside ψ_{Crit} have average bad curvature, and are MHD-unstable. All flux surfaces studied in this work are either absolute- or average-MHD-stable.

2.2. General Plasma Diagnostics

2.2.1. Plasma Density - n

The principal diagnostic for plasma particle density is a vertical path multiradian fringe-shift 70 GHz microwave interferometer[23] located on the Octupole's midcylinder. Properly this measures $\int n_e \, dl$. Since the volume sampled is dominated by the separatrix region of flux space, the interferometer is taken as a measure of the separatrix (peak) density. This is only slightly affected by changes in density profile.

The (ion) density profile is measured using Langmuir floating double probes.[24] The probes used in these studies consisted of 1 mm-dia. platinum spheres protruding from a ceramic stalk. The spheres were ~ 3 mm apart, and were typically biased apart by 100 V. The measured saturation current is predicted to vary as

$$I_s \propto n_i T^{1/2}, \qquad (2\text{-}1)$$

where T is the greater of T_i and T_e. In order to determine the density profile from saturation current measurements, the temperature must be separately determined (see below). For these experiments, $T_i \approx T_e$ as measured, consequently T_e has typically been used to unfold probe density measurements. The proportionality factor in Eq. 2-1 is obtained by normalizing the density profile (from the probe) to the interferometer density.

2.2.2. Electron Temperature - T_e

The electron temperature is measured using, almost exclusively, the admittance probe technique of J.C. Sprott.[25] For this diagnostic, a third tip was built into the floating double Langmuir probe, identical to the other two. This tip is connected to a 400 kHz capacitive bridge, and used to measure the plasma-tip sheath impedence, R_s. The electron temperature (in eV) is then given, from probe theory, as

$$T_e = e \, I_s \, R_s .$$

The admittance signal from the capactive bridge is demodulated using the active full-wave rectifier in Fig. 2-3, and the resulting signal and the saturation current (from the floating double probe) are recorded to give T_e versus time at the probe position for each shot.

In addition, principally during the high-β studies[13,14] the electron temperature was also determined by measuring the slope of a double probe I-V characteristic at the floating potential.[24] The temperature determined in the two ways agreed to within 10% independent of plasma

parameters.

2.2.3. Ion Temperature - T_i

The ion temperature is measured using a 1/4-inch-diameter gridded electrostatic analyzer probe.[26] The analyzer consists of three gold grids and a collector, each separated by 127 μm mica washers, assembled in a technique developed by P. Nonn.[27] The first grid is allowed to float, and the other grids are biased relative to it. This grid prevents the penetration of the discrimination potentials into the plasma, eliminating particle acceleration problems encountered with "skimmer" probes.[28] The second grid is biased to repel ions, and the bias is varied (either shot to shot, or in a fast sweep) to accept different (upper) portions of the ion distribution function. The collector is biased to collect all the ions passing the second grid, while the third grid serves as a secondary electron supressor. The ion temperature (for singly charged ions) is given by

$$T_i = -\left[\frac{d\ln I_c}{dV_2}\right]^{-1}$$

where V_2 is the discrimination bias voltage on the second grid and I_c is the collector current.

2.3. Plasma Current Diagnostics

Separate methods are used to measure the ion current density and the total current density (ions and electrons). However, in each technique, the poloidal and toroidal current densities are measured on

separate shots. In order to compare the currents to theory, as done in chapter 4, both j_P and j_T are required (they are resolved into $j_\perp$ and $j_\parallel$). This is done by picking pairs of shots (each measuring a different current component) that are matched in their plasma kinetic parameters (T_e and n_e), and the time decay of those parameters. The plasma parameters are matched for the separatrix, and the flux surface where the currents are measured (if different than the separatrix). For studies involving current measurements in different locations (e.g. to measure poloidal variation) or different field configurations (e.g. B_T scans), the pairs of matched shot are further matched to give an overall compatible set.

2.3.1. Ion Current - J_i

The local ion current density is measured using a "paddle probe".[29, 10] This probe consists of two parallel flat disks separated by a thin insulator. Each disk is biased to collect ion saturation current as a single Langmuir probe. The difference in the collected currents is equal to the directed ion current flowing perpendicular to the disks.[29] For these experiments, the disks are platinum of diameter 3.2 mm, the insulator is alumina and Sauereisen[30] cement No. 29, providing a separation of 1 mm. Great care must be taken during assembly to ensure that the disks are parallel. Typical disk bias voltage is -100 V. The currents collected by the tips are measured as voltages across matched 5 Ω resistors. The difference current is measured using an AM502 differential amplifier.

It was originally expected that this probe should be capable of measuring the directed electron current, by biasing the disks to collect electron saturation current. However, an apparent probe-sheath instability occured for bias potentials above the plasma potential, making operation of the probe difficult. Attempts to operate the probes in electron saturation also appeared to cause permanent damage to the surface of the platinum disks.

2.3.2. Total Current - J

A method of measuring the total current density, using multi-coil magnetic probes and active integrators, was developed in the course of these studies. This method will be described in some detail.

2.3.2.1. Experimental Method

For an axisymmetric toroidal system expressions for the current density may be obtained from the components of $\mu\vec{J}=\nabla\times\vec{B}$, giving

$$\mu J_P = \nabla_\psi B_T - \hat{\chi}\cdot\left[\vec{B}_T\times\frac{\hat{R}}{R}\right], \tag{2-2}$$

$$\mu J_T = -(\nabla_\psi B_P + \kappa_P B_P), \tag{2-3}$$

where the P and T subscripts denote poloidal and toroidal components respectively, $\nabla_\psi\equiv\hat{\psi}\cdot\nabla$, $\hat{\psi}$ is the unit normal to the magnetic flux surface, $\hat{\chi}$ is the unit vector in the poloidal direction, R is the major radius, and κ_P is the local curvature of the poloidal field. The sign of κ_P is taken as positive if the poloidal field is curving towards the magnetic axis (as in a tokamak), and negative otherwise. Eq. (2-2) can be simplified in the

particular cases where the flux surface is locally horizontal:

$$\mu J_P = \nabla_\psi B_T, \tag{2-4}$$

or vertical:

$$\mu J_P = \nabla_\psi B_T \pm \frac{B_T}{R}, \tag{2-5}$$

where the positive sign applies to the outside of the torus, and the negative to the inside.

In the case where the curvature of a component of the field is not significantly perturbed by the plasma (i.e. B_T in all devices, B_P in multipoles) increased sensitivity to the *conjugate* current may be obtained by measuring the plasma perturbation to the above equations, giving

$$\mu J_T = -\delta(\nabla_\psi B_P) - \kappa_P\,\delta B_P - B_P\,\delta\kappa_P,$$
$$\simeq -\delta(\nabla_\psi B_P) - \kappa_P\,\delta B_P, \tag{2-3'}$$

$$\mu J_P = \delta(\nabla_\psi B_T), \tag{2-4'}$$

$$\mu J_P = \delta(\nabla_\psi B_T) \pm \frac{\delta B_T}{R}, \tag{2-5'}$$

where δ indicates the difference between the quantity measured with plasma and without.

In the present experiment, $\partial_t B$ and $\partial_t\nabla_\psi B$ are measured using two parallel magnetic loops, displaced in the $\hat{\psi}$ direction. The difference between the loops' signals (divided by their separation distance) is taken as the approximate measure of the field gradient. A set of active integrators, gated and non-gated as described below, integrates each signal producing outputs proportional to B and $\nabla_\psi B$ during each discharge. The non-gated integrators measure the total B and $\nabla_\psi B$ during the entire

machine pulse. The gated integrators are enabled either just before or after plasma injection, near peak field, and thus do not measure most of the background magnetic field strength, and have higher gain than the non-gated integrators. δB and $\delta\nabla_\psi B$ are obtained by (computer) subtraction of the gated integrator outputs for a non-plasma shot from the outputs for a plasma discharge. κ_P may be determined from Eq. (2-3) using the B and $\nabla_\psi B$ outputs on non-plasma shots ($J_T = 0$), with the probe oriented to measure poloidal field. The current density component is obtained from Eqs. (2-3'), (2-4'), or (2-5') depending on the orientation and location of the probe.

2.3.2.2. Apparatus: Field Probes

The magnetic probes used in these experiments contain two or more parallel coils (Fig. 2-4). The coil separations used to date are 0.6 cm and 1.0 cm. The two components of the current, J_T and J_P, are obtained on separate shots with the probe aligned to measure B_P and B_T respectively. The coils are wound of ~110 turns of #42 copper magnet wire, on a machined G10 coil form, with a coil cross section of 2.5 mm × 5.0 mm. The coil assembly is electrostaticaly shielded by encasing it with a layer of 13 μm-thick aluminum foil, and inserting into a 5/32 in.-I.D., 0.13 mm-wall, 4 cm long stainless steel sleeve which has been soldered onto a thick-wall 1. m long, 5/32 in.-O.D. stainless steel tube. The stainless tube, with coils, is then inserted into a 1/4 in.-O.D. pyrex or quartz tube which electrically insulates the shield from the plasma, and is closed at

the end to provide the vacuum seal.

The probe is coupled to the integrators using a shielded multi-twisted-pair cable. The cable shield is connected to the probe electrostatic shield, and is grounded in the integrator. For maximum sensitivity, it is necessary to avoid connectors (e.g. BNC or LEMO) in coupling the coils to the integrators, as they introduce significant noise. In this experiment solder lugs and screw type connector blocks were used, mounted inside the integrator's shield box.

2.3.2.3. Apparatus: Active Integrators

The active circuitry consists of front-end amplifiers and the integrating amplifiers. The differential and single-ended front-end amplifiers, for measurements of $\nabla_\psi B$ and B respectively, are shown in Fig. 2-5. The front-end amplifiers are required by the need for a high input impedance (as seen by the probe) for good frequency response, and a differential input (for the gradient measurement). The OP-37 operational amplifier[31] was chosen for its relatively high bandwidth, low offset and drift, low noise, and especially its low noise corner (2.7 Hz). The front-end amplifiers are configured to be flat to ≃1.7 MHz, and the differential amplifier has 80 dB CMRR at 100 KHz. The gain of the front-end amplifiers is maximized, while not imparing bandwidth or saturating, to minimize the effect of the low frequency input noise of the integrating amplifiers.

The schematic for the gated and non-gated integrating amplifiers is shown in Fig. 2-6. The input capacitive coupling eliminates any output offset of the front-end amplifiers, but has a time constant ($\geq$1. sec) long enough to pass signals of experimental interest. It is still necessary to use low output offset front-end amplifiers, to minimize the leakage current through the coupling capacitors. The ICL7650 chopper-stabilized operational amplifier[32] was chosen for the non-gated integrating amplifiers because of its extremely low input offset (1.0 μV), low drift, and low bias current ($\simeq$ 0.1 pA). Note that for the gated integrator, the internal chopping clock ($\simeq$ 200 Hz) is disabled during the integration period to limit generation of switching noise. However, the noise corner of the ICL7650 ($\simeq$ 1.5 KHz) will limit the sensitivity of high gain integrators. The variable gain of the gated integrator is generated in the feedback loop of the integrating amplifier, avoiding the gain dependent high-frequency rolloff that would be generated in a variable gain output amplifier. The switchable output offsets (±4V, 0V) allow better utilization of the input range of our digitizers (±5V) for unipolar signals. The fixed gain of $\simeq$2 in the offset amplifiers maps the saturated range of the ICL7650 (±4.7V) onto the potential ±9V range needed for unipolar signals.

All active circuitry was mounted in a grounded conducting box, to shield out stray fields. Incoming AC power was isolated and filtered. To avoid picking up stray 60 Hz and 180 Hz fields *in the active circuits* it is necessary to mount all power transformers away from the circuitry and

outside the shield box, in their own shield.

2.3.2.4. Performance

With the described apparatus, we are able to measure the plasma perturbation to the magnetic field with a resolution of $\simeq$6 mG/cm, corresponding to a current density resolution of $\simeq$5 mA/cm^2, in a field of 1 kG with a vacuum gradient of $\simeq$70 G/cm. An example experimental diamagnetic current profile is shown in Fig. 2-7 with the expected profile computed from the experimental pressure profile measured by double Langmuir probes.

2.4. Plasma Parameters

The "Intermediate" Marshall gun[33] was used to generate all of the plasma used in these studies. The gun's energy storage bank consists of 60 μF at 20 kV, and is switched by a spark gap through about 30 nH to drive the gun. Typical plasma parameters are summarized in Table 2-2. This plasma was obtained with the gun's capacitor bank charged to 14 kV, the gas plenum filled with H_2 to 50 psig, and a 400 μsec valve-to-gun time delay. It was chosen to have a reasonably high β, 2%, (to make the currents large enough to measure) while not causing large distortions in the flux surface positions (for ease of analysis). In addition, this plasma was chosen to satisfy the assumptions of neoclassical theory (small gyroradii), and have diamagnetic current which agrees in magnitude and spatial structure with theory, in contrast to some of the plasmas in

Table 2-2

Typical Plasma Parameters for this Experiment

$n_e \sim 1\times10^{13}\ cm^{-3}$ @ 400μsec after injection

$T_i \sim T_e \sim 17$–$21\ eV$ @ 400μsec

$B_T \lesssim 500$ G

$B_P = 860$ G on separatrix in outer high field region

$\tau_\beta \sim 1$ msec, β decay time

Alfvén time ~ 0.1 msec

Reference (13). The "Big" guns[34] were avoided, due to their low temperatures, and the relatively large low frequency fluctuations present at "low" densities ($1.0\times10^{13}\ cm^{-3}$).

Since the magnetic field is pulsed inductively, and the boundary currents flow in finite conductivity metal, the magnetic field changes in time, with a fundamental frequency of 11 Hz. In order to minimize the effect of the resulting electric fields on this experiment, the plasma is injected into the device ~ 1 msec before the measured peak of the field. Thus, by the time the plasma current flow equilibrates, $\vec{E} = 0$. Since the toroidal and poloidal magnetic fields are generated independently, and are always of slightly different period, they must be triggered at different times in order to align their peaks. This is necessary to minimize the changing of the magnetic field pitch during the experiment. Currently,

the toroidal field must be triggered ~ 1.2 msec after the poloidal field. the poloidal field peaks at 19.4 msec, and the gun is fired at 18.4 msec.

Typical profiles of n_i and p are shown in Figs. 2-8. Fig. 2-9 shows the time decay of the peak (separatrix) density and temperature after gun injection. Profiles of $\frac{n_i'}{n_i}$ and $\frac{T_e'}{T_e}$ are shown in Figs. 2-10 and 2-11. Calculated time evolution of the local beta (in the high-field region) and electron-electron mean free path are shown in Fig. 2-12.

Fig. 2-1. Wisconsin Levitated Octupole.

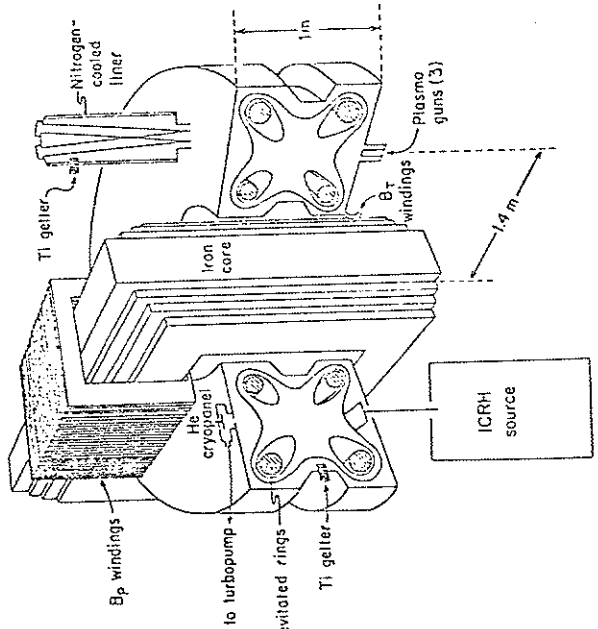

Fig. 2-2. Poloidal flux plot of octupole superimposed on outline of boundary conductors.

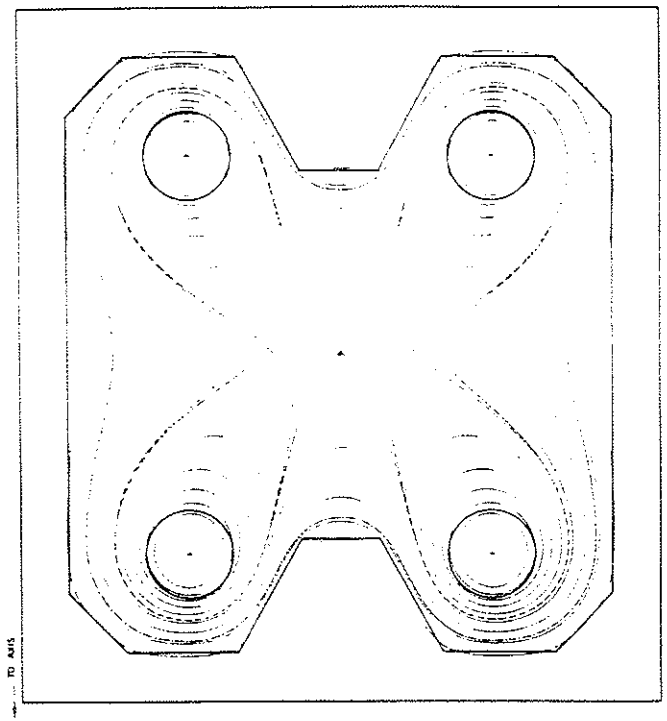

Fig. 2-3. Active full-wave rectifier circuit used to demodulate signal from admittance bridge.

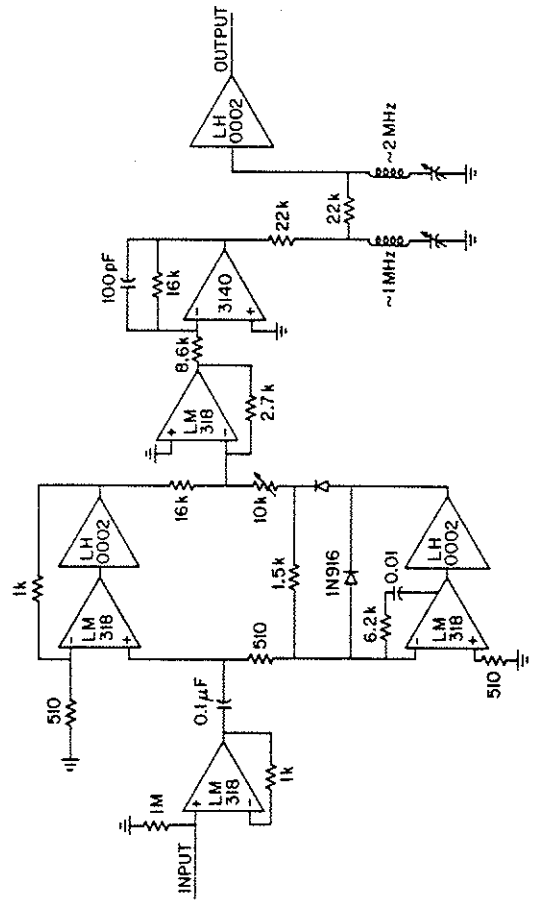

Fig. 2-4. Dimensions of coil form used for two-coil magnetic probe. Coils are parallel, separated by 0.5 cm.

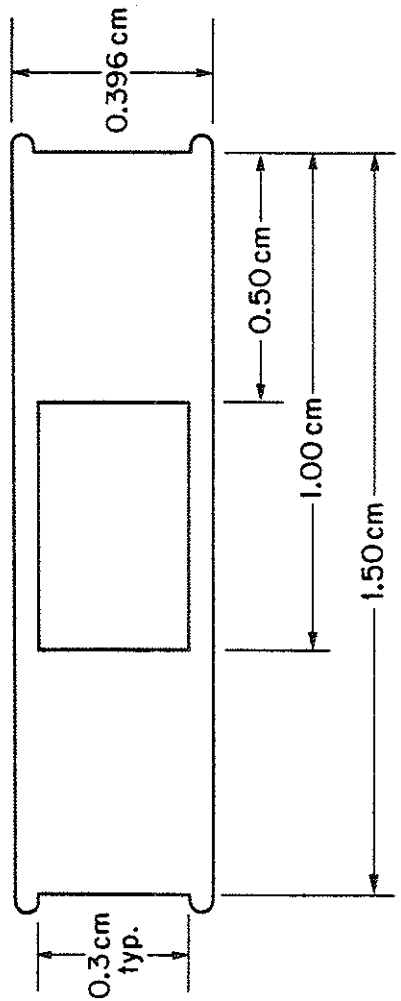

Fig. 2-5. Schematic of front-end amplifiers, used to buffer signals from pick-up coils, and prepare signal for integrating amplifiers. The single ended amplifier is used for measurements of B from a single coil. The differential amplifier is used to measure ∇B using two coils.

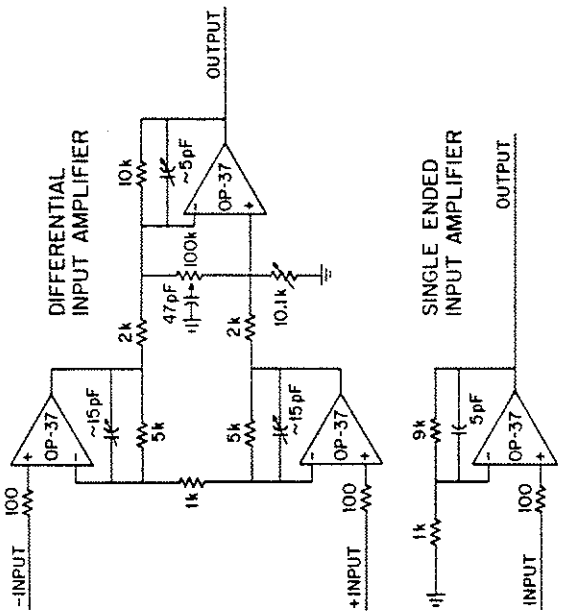

Fig. 2-6. Integrating amplifiers. The non-gated integrator is used to measured the total magnetic field. The gated integrator ignores most of the vacuum field, giving higher sensitivity to the plasma perturbation.

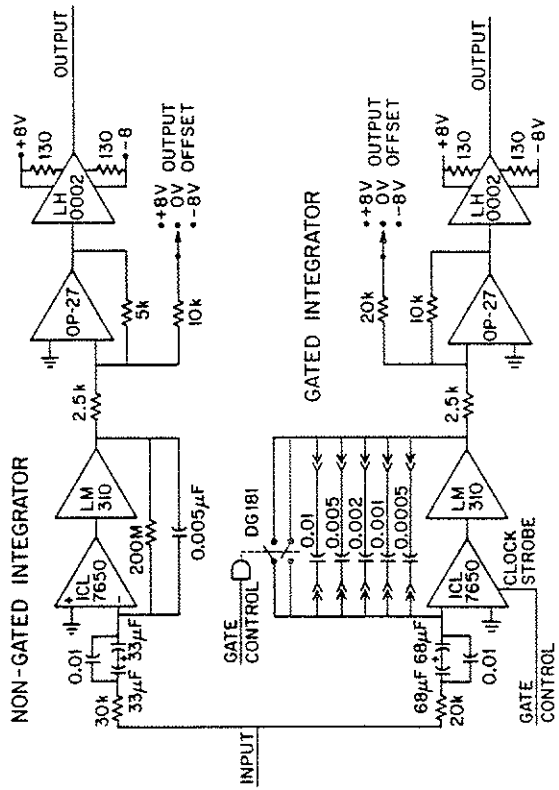

Fig. 2-7. Measured diamagnetic current profile (points) and calculated profile (curve) from experimental pressure profile measured by Langmuir probes.

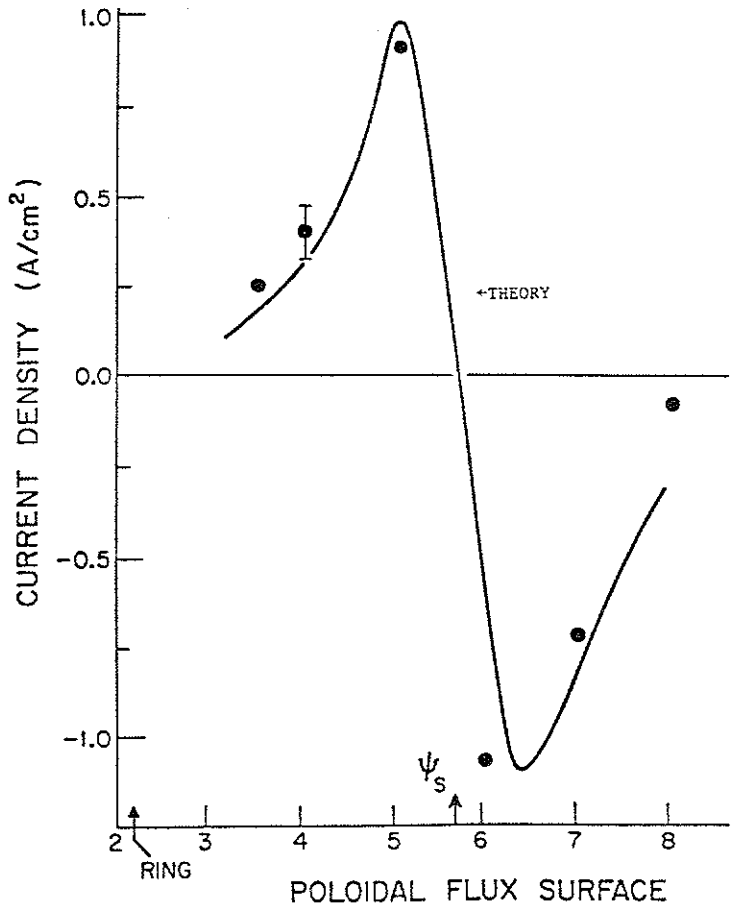

Fig. 2-8. Typical density and pressure profile for plasmas studied, at 400 μsec after gun injecton.

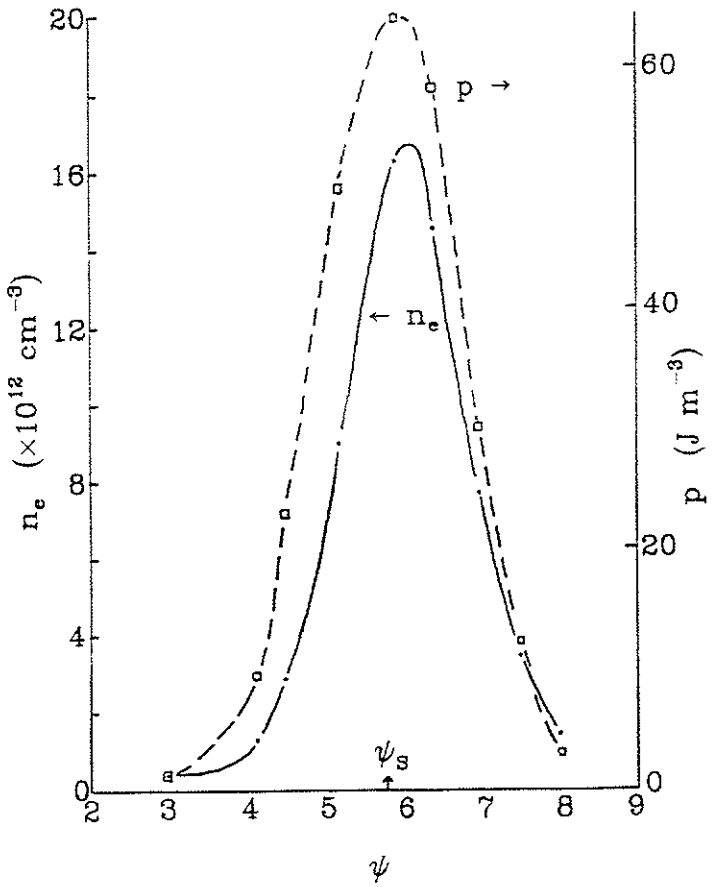

Fig. 2-9 Typical time decay of n_e and T_e after injection, measured by interferometer and Lanmuir probes, respectively.

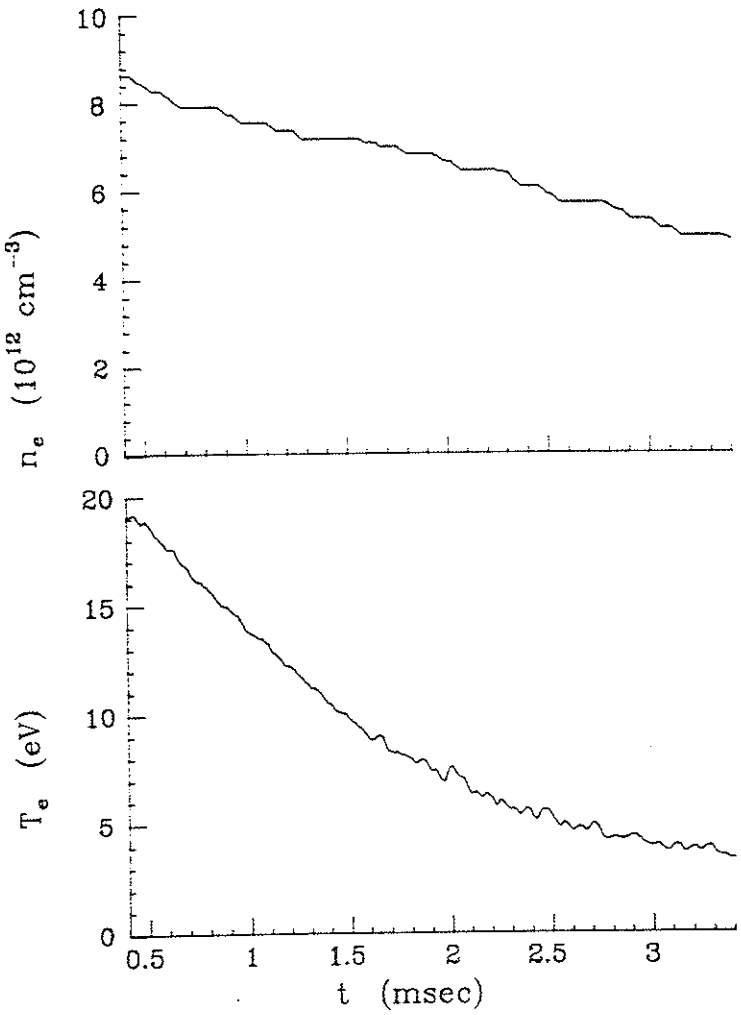

Fig. 2-10. Typical profile of $\nabla n_i / n_i$ at 500 μsec after injection, measured with Langmuir probe.

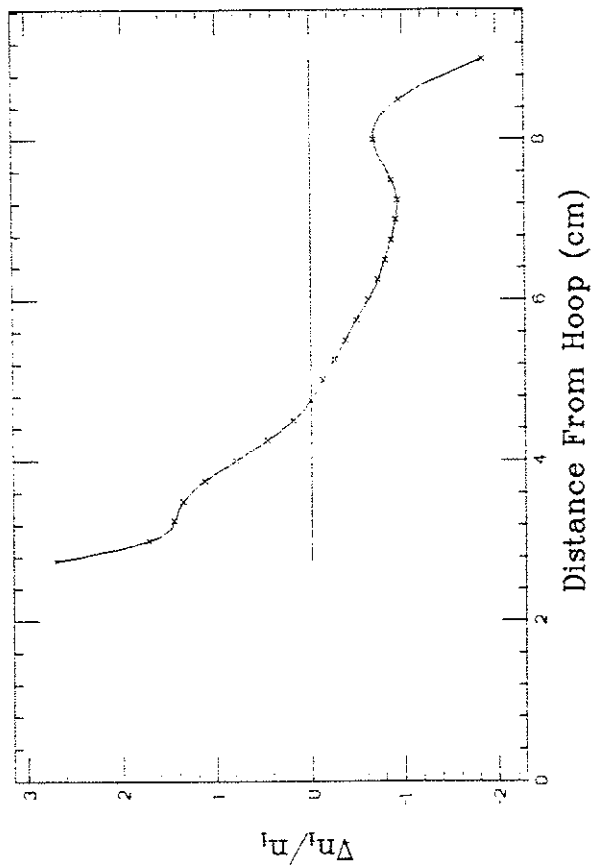

Fig 2-11. Typical profile of $\nabla T_e / T_e$.

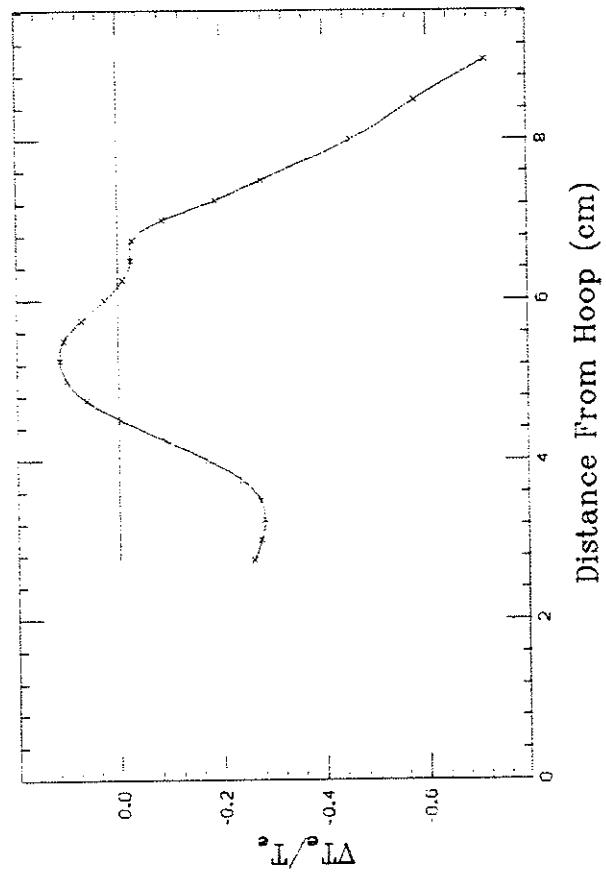

Fig. 2-12. Time decay of local β_e (in outer high field region, on separatrix), and separatrix mean-free-path, λ_{ee}.

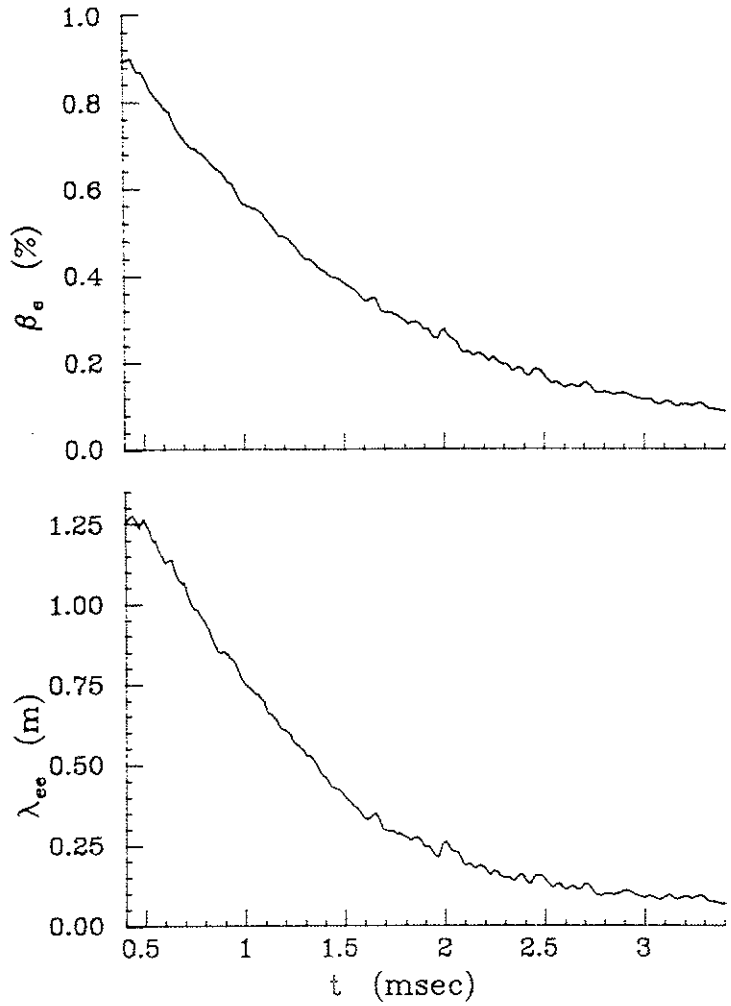

Chapter 3

Theory of Neoclassical Currents

The original kinetic-theory formulations of neoclassical transport theory[1,2] were restricted to large aspect ratio configurations with circular, and later elliptical, flux surfaces. Relatively recently, Hirshman and Sigmar's moment equation approach[15] has allowed calculation of neoclassical effects in axisymmetric geometries of arbitrary cross section. This chapter includes a physical explanation of the neoclassical current, a summary of the moment equation approach for calculating the current for a simple hydrogen plasma (following Hirshman and Sigmar, and related papers), and application of this approach to the experimental geometry.

Throughout this chapter the coordinate system illustrated in Fig. 3-1 shall be used.

3.1. Equilibrium Current Structure

In a magnetized plasma, the pressure gradient perpendicular to the magnetic field is balanced by the confining (diamagnetic) current

$$\vec{j}_\perp = \frac{\vec{B}\times\nabla p}{B^2},$$

where p is the total plasma kinetic pressure. For an axisymmetric system with closed magnetic flux surfaces, such as the experimental configuration, this can be simplified to

$$j_\perp = R\,p'\,\frac{B_P}{B},$$

where $'$ denotes $\partial/\partial\psi$. In steady-state, to avoid local charge accumulation $\nabla\cdot\vec{j}=0$, implying $\nabla\cdot\vec{j}_\perp = -\nabla\cdot\vec{j}_\parallel$. For an axisymmetric toroidal system with helical magnetic field $\nabla_\perp B \neq 0$, thus

$$\nabla\cdot\vec{j}_\perp = -R\,p'\,B_T B_P \nabla_\chi B^{-2}, \text{ and}$$

$$\nabla\cdot\vec{j}_\parallel = \nabla\cdot\left[\frac{(\vec{j}\cdot\vec{B})\,\vec{B}}{B^2}\right]$$

$$= (\vec{B}\cdot\nabla)\left(\frac{\vec{j}\cdot\vec{B}}{B^2}\right)$$

$$= B_P \nabla_\chi\left(\frac{\vec{j}\cdot\vec{B}}{B^2}\right).$$

Substituting these expressions into $\nabla\cdot\vec{j}_\perp = -\nabla\cdot\vec{j}_\parallel$, integrating poloidally, and using the fact that p' and $F(\psi)=RB_T$ are flux surface constants (properly only to first order in the Larmor-radius expansion done below) gives

$$j_\parallel = F\,\frac{p'}{B} + BK(\psi), \tag{3-1}$$

where $K(\psi)$ is the flux-surface-constant of integration. The first term provides for current continuity with $j_\perp$, while the second represents additional divergenceless flow, which is indeterminate at this point.

Additional insight may be gained by forming the toroidal and poloidal components of the current:

$$j_T = Rp' + B_T K(\psi),$$

$j_P = B_P K(\psi)$.

The first term of j_T confines ∇p as if B_T were zero, while $K(\psi)$ gives the amount of poloidal current.

3.2. Simplified Calculation of Neoclassical Parallel Current

$K(\psi)$, and thus $j_\parallel$, is determined from the steady state fluid force balance equations. A simplified, but inaccurate, partial derivation of the current is presented first, to elucidate the physics involved. This is followed by a more complete calculation, resulting in the expressions that are compared to the experiment.

Consider the electron fluid momentum balance equation (the $\vec{v}$ moment of the Vlasov equation)

$$0 = n_e e_e (\vec{E} + \vec{u}_e \times \vec{B}) - \nabla p_e - \nabla \cdot \vec{\pi}_e + \vec{R}_e \ , \tag{3-2}$$

where $n_e = \int f_e \, d\vec{v}$ is the density, $e_e = -|e|$ is the electron charge, $u_e = n_e^{-1} \int \vec{v} f_e \, d\vec{v}$ is the flow velocity, p_e is the electron kinetic pressure,

$$\vec{\pi}_e = \int m_e \left[(\vec{v}-\vec{u}_e)(\vec{v}-\vec{u}_e) - |\vec{v}-\vec{u}_e|^2 \frac{\vec{I}}{3} \right] f_e \, d\vec{v}$$

is the traceless viscosity tensor, m_e is the electron mass, $\vec{R}_e = \int m_e \vec{v} C_e \, d\vec{v}$ is the friction force, f_e is the distribution function, C_e is the operator describing collisions between electrons and all particle species, and the subscript e is the species index indicating electrons. Taking the flux-surface-average of the parallel component yields

$$\langle \vec{B} \cdot \nabla \cdot \vec{\pi}_e \rangle = \langle \vec{B} \cdot \vec{R}_e \rangle - n_e e \langle \vec{B} \cdot \vec{E} \rangle \ . \tag{3-3}$$

where

$$\langle A \rangle = \frac{\int \frac{A}{B} dL_\parallel}{\int \frac{dL_\parallel}{B}} .$$

Eq. 3-3 is recognized as the classical flux-surface-averaged Ohm's Law, with the parallel viscosity term retained. The bootstrap current will turn out to be proportional to the viscosity (in this simplified calculation). Classically, the parallel friction is given by[35]

$$\langle \vec{B} \cdot \vec{R}_e \rangle = \frac{n_e e}{\sigma_S} \langle \vec{B} \cdot \vec{j} \rangle \tag{3-4}$$

where σ_S is the Spitzer-conductivity, giving

$$\langle \vec{B} \cdot \vec{j} \rangle = \sigma_S \langle \vec{B} \cdot \vec{E} \rangle + \frac{\sigma_S}{n_e e} \langle \vec{B} \cdot \nabla \cdot \vec{\pi}_e \rangle \ . \tag{3-5}$$

This expression neglects contributions to $\langle \vec{B} \cdot \vec{R}_e \rangle$ proportional to the heat flow and higher order flows (which will be considered in the next section). Inclusion of additional flows will introduce additional terms to Eq. 3-5 and require simultaneous solutions of additional equations (e.g., the heat flux balance equation). However, many of the characteristics of neoclassical currents are evident in the simple structure of Eq. 3-5.

When $\langle \vec{B} \cdot \vec{E} \rangle \neq 0$ the ohmic current is reduced by the parallel viscous force, due (in the collisionless regime) to the well known lack of current carried by trapped particles.[36]

With $\langle \vec{B} \cdot \vec{E} \rangle = 0$, Eqs. 3-1 and 3-5 give

$$j_\parallel = \frac{F p'}{B} \left(1 - \frac{B^2}{\langle B^2 \rangle} \right) + \frac{\sigma_S}{n_e e} \frac{B \langle \vec{B} \cdot \nabla \cdot \vec{\pi}_e \rangle}{\langle B^2 \rangle} . \tag{3-6}$$

In the limit $\nu_e \to \infty$, collisions are so frequent that any deviation of the dis-

tribution function from a Maxwellian is washed out, and $\langle \vec{B}\cdot\nabla\cdot\vec{\pi}_e \rangle = 0$. Thus, there is no net force on the flux surface, and from Eqs. 3-3 and 3-4 $\langle \vec{B}\cdot\vec{j} \rangle \propto \langle \vec{B}\cdot\vec{R}_e \rangle = 0$. In Eq. 3-6, only the first term remains, giving the Pfirsch-Schlüter current[7] consisting of the term necessary for current continuity, and a term to ensure $\langle \vec{B}\cdot\vec{J} \rangle = 0$.

The second term in Eq. 3-6 is the bootstrap current, a divergenceless unidirectional current driven directly by the parallel viscosity. It will turn out that the parallel viscosity is proportional to the poloidal component of the particle flows (and heat flows), and attempts to limit plasma poloidal rotation. In the collisional regime, this is due to the compressional work done on the plasma, as it passes into high field (narrow flux-tube) regions. In the collisionless (banana) regime, this is due to like-particle collisions between (flowing) untrapped particles, and (no-net-flow) trapped particles. In the limit where the parallel viscosity becomes very large (high poloidal mirror ratio), the plasma will establish the level of parallel current so that the total current (including the perpendicular confining current) is only toroidal, as in Fig. 3-2.

3.3. Detailed Calculation of Neoclassical Currents

To accurately calculate the collisionality dependence of the neoclassical current, and the partition of the current between ions and electrons, the friction and viscous forces must be carefully calculated from kinetic theory. To present a unified treatment, we start from the drift-kinetic-equation(DKE), which is the gyrophase averaged Vlasov equation

for small $\delta = \rho/l$, where ρ is the gyroradius and l is the gradient scale length. This equation is approximately solved by first expanding the distribution function in δ, and then expanding the remaining $v_\parallel$ and v dependence of the distribution function in Legendre and Laguerre polynomials[37] respectively. The first several coefficients of these expansions are readily identified with various fluid variables (e.g., velocities, viscosities). Inserting these expansions back into the DKE generates an infinite sequence of coupled ordinary differential equations (only parallel spatial derivatives remain unevaluated) in the expansion coefficients. The first several of these equations are identified as various parallel fluid equations (e.g., parallel continuity and parallel force balance equations). By truncating the expansions, and the sequence of equations, a (small) set of equations is obtained, involving only the fluid variables (flows and viscosities) and moments of the collision operator. These moments and viscosities are then evaluated in terms of the fluid flows. The viscosities are calculated analytically in several asymptotic collisionality regimes, using various approximate forms of the DKE, and are "smoothed" together to give expressions for arbitrary collision frequency. Thus the fluid equations (from the infinite sequence) only involve the balance of the fluid flows, and are finally solved directly for the flow velocities of the individual species, and thus the current.

The steady state DKE[38] for each species (a) is

$$(v_\parallel + v_{Da})\cdot\nabla \bar{f}_a - \frac{e_a}{m_a} v_\parallel \cdot \partial_t \vec{A}\, \frac{\partial \bar{f}_a}{\partial \varepsilon} = \sum_b C_{ab}(\bar{f}_a, \bar{f}_b) \qquad (3\text{-}7)$$

where $\vec{v}_{Da}$ is the perpendicular drift velocity, $\bar{f}_a$ is the gyrophase averaged distribution function, $\vec{A}$ is the vector potential, $\varepsilon = \frac{1}{2}m_a v^2 + e_a\Phi(\psi)$ is the total particle energy and a constant of the motion, $\Phi(\psi)$ is the electrostatic potential, C_{ab} is the collision operator between species a and b. Terms of the DKE given in Reference (38) that were clearly $O(\delta^2)$ have been neglected, and $\beta = O(\delta)$. We shall drop the overbar notation, and all distribution functions shall be understood to be gyrophase averaged. Expanding f_a as $f_{a0}+f_{a1}$, where $f_{a1}/f_{a0} = O(\delta)$, and substituting into Eq. 3-7 gives the $O(\delta^0)$ equation

$$\vec{v}_{\parallel}\cdot\nabla f_{a0} = \sum_b C_{ab}(f_{a0}, f_{b0}) .$$

The solution for the lowest order distribution function is a local Maxwellian[2]

$$f_{a0} = \frac{n_a(\psi)}{\pi^{3/2} v_{Ta}^3} e^{-x_a^2} ,$$

where $v_{Ta} = (2T_a(\psi)/m_a)^{1/2}$ is the thermal speed, and $x_a = v/v_{Ta}$. The $O(\delta)$ equation is

$$\vec{v}_{\parallel} f_{a1} + \vec{v}_{Da}\cdot\nabla\psi f_{a0} - v_{\parallel}\frac{e_a E_{\parallel}}{T_a} f_{a0} = C_a(f_{a1}, f_{b1}) , \tag{3-8}$$

where

$$C_a(f_{a1}, f_{b1}) = \sum_b [\, C_{ab}(f_{a1}, f_{b0}) + C_{ab}(f_{a0}, f_{b1})\,] \tag{3-9}$$

is the collision operator linearized about the Maxwellian f_{a0}, and $\vec{n} = \vec{B}/B$. The perpendicular drift velocity is given (for the geometry in Fig. 3-1) by[39]

$$\vec{v}_{Da}\cdot\nabla\psi = -F(\psi) v_{\parallel}(\vec{n}\cdot\nabla)\left(\frac{v_{\parallel}}{\Omega_a}\right) , \tag{3-10}$$

$$= F(\psi)\frac{(\vec{n}\cdot\nabla B)}{e_a B^2}\frac{m_a}{2}(v_{\parallel}^2 + v_{\perp}^2) ,$$

where $\Omega_a = e_a B/m_a$ is the cyclotron frequency.

In order to separate out the $v_{\parallel}$ dependence, f_{a1} is expanded in Legendre polynomials:

$$f_{a1} = f_{a0}\sum_l A_{al}(\psi, \chi, v) P_l\left(\frac{v_{\parallel}}{v}\right) ,$$

where $P_0 = 1$, $P_1(x) = x$, and $P_2(x) = \frac{1}{2}(3x^2 - 1)$. When this expansion is inserted into Eq. 3-8, and the identities $(\vec{n}\cdot\nabla)_{\varepsilon,\mu} v_{\perp}^2 = -v_{\perp}^2(\vec{n}\cdot\nabla B)/B$ and[40]

$$(1-x^2)\frac{dP_l(x)}{dx} = \frac{l(l+1)}{2l+1}(P_{(l-1)}(x) - P_{(l+1)}(x))$$

are used, an infinite sequence of coupled differential equations of the form

$$\begin{aligned} C_a^{(l)}(A_{al}, A_{bl}) = {} & v\frac{l}{2l-1}\left[\frac{(l-1)}{2}\frac{\vec{n}\cdot\nabla B}{B} + \vec{n}\cdot\nabla\right] f_{a0} A_{a(l-1)} \\ & + v\frac{l+1}{2l+3}\left[-\frac{(l+2)}{2}\frac{\vec{n}\cdot\nabla B}{B} + \vec{n}\cdot\nabla\right] f_{a0} A_{a(l+1)} \\ & - v\frac{e_a E_{\parallel}}{T_a}\delta_{l1} f_{a0} \\ & + F\frac{\vec{n}\cdot\nabla B}{e_a B^2} T_a x_a^2\left(\frac{4}{3}\delta_{l0} + \frac{2}{3}\delta_{l2}\right) f_{a0} , \end{aligned} \tag{3-11}$$

are generated, where δ_{lm} is the Kronecker delta, and

$$C_a^{(l)}(A_{al}, A_{bl}) P_l \equiv C_a(A_{al} P_l f_{a0}, A_{bl} P_l f_{b0}) ,$$

since the Legendre polynomials (indeed all spherical harmonics) are eigenfunctions of the linearized collision operator[41] (partially motivating

this expansion). Further expanding the v dependence of A_{a1} in Laguerre polynomials of order 3/2

$$A_{a1} = \frac{2}{v_{Ta}} x_a \sum_j u_{aj}(\psi,\chi) L_j^{(3/2)}(x_a^2) \tag{3-12}$$

$$u_{aj} = \frac{v_{Ta}}{2} \frac{\int x_a L_j^{(3/2)}(x_a^2) P_1(\frac{v_\parallel}{v}) f_{a1} d\vec{v}}{\int x_a^2 [L_j^{(3/2)}(x_a^2) P_1(\frac{v_\parallel}{v})]^2 f_{a0} d\vec{v}}$$

where $L_0^{(3/2)}=1$ and $L_1^{(3/2)}(x_a^2)=\frac{5}{2}-x_a^2$, the first two coefficients are identified as

$$u_{a0} = \vec{n}\cdot\vec{v}_a = u_{\parallel a} ,$$

$$u_{a1} = -\frac{2}{5}\frac{\vec{n}\cdot\vec{q}_a}{p_a} = -\frac{2}{5}\frac{q_{\parallel a}}{p_a} ,$$

where $\vec{q}_a = -T_a \int L_1^{(3/2)} \vec{v} f_{a1} d\vec{v}$ is the thermal (random) heat flux.

Thus, to calculate the parallel current we must solve a suitably truncated Eq. 3-11 for each $u_{\parallel a}=u_{a0}$ (i.e. for each species) eliminating all other expansion coefficients of the distribution functions. These equations have recently been solved numerically for the ion heat conductivity in a simple large aspect ratio circular cross section tokamak, by expanding the parallel spatial dependence in a Fourier series.[8] In the moment approach, analytic solutions are obtained in various asymptotic collisionality regimes, and then smoothed together to get a continuously valid approximation.

Expanding A_{a0} in Laguerre polynomials of order 1/2 gives

$$A_{a0} = \sum_j n_{aj} L_j^{(1/2)}(x_a^2) , \tag{3-13}$$

$$n_{aj} = \frac{\int L_j^{(1/2)}(x_a^2) P_0 f_{a1} d\vec{v}}{\int [L_j^{(1/2)}(x_a^2) P_0]^2 f_{a0} d\vec{v}} ,$$

where $L_0^{(1/2)}=1$, $L_1^{(1/2)}(x_a^2)=\frac{3}{2}-x_a^2$. The first two coefficients are identified as

$$n_{a0} = \tilde{n}_a ,$$

$$n_{a1} = -\tilde{T}_a \frac{n_a}{T_a} ,$$

where $\tilde{n}_a$ and $\tilde{T}_a$ are the poloidally varying portions of the density and temperature, respectively. Expanding A_{a2} in Laguerre polynomials of order 5/2

$$A_{a2} = \frac{2}{3} x_a^2 \sum_j p_{aj}(\psi,\chi) L_j^{(5/2)}(x_a^2) . \tag{3-14}$$

$$p_{aj} = \frac{3}{2} \frac{\int x_a^2 L_j^{(5/2)}(x_a^2) P_2(\frac{v_\parallel}{v}) f_{a1} d\vec{v}}{\int x_a^4 [L_j^{(5/2)}(x_a^2) P_2(\frac{v_\parallel}{v})]^2 f_{a0} d\vec{v}} .$$

where $L_0^{(5/2)}=1$, $L_1^{(5/2)}(x_a^2)=\frac{7}{2}-x_a^2$. The first two coefficients are identified as

$$p_{a0} p_a = p_{\parallel a} - p_{\perp a} ,$$

$$p_{a1} p_a = -\frac{2}{7}(\Theta_{\parallel a} - \Theta_{\perp a}) + \frac{2}{7} p_{a0} p_a ,$$

where $p_{\parallel a} = \int m_a v_\parallel^2 f_{a1} d\vec{v}$, $p_{\perp a} = \int \tfrac{1}{2} m_a v_\perp^2 f_{a1} d\vec{v}$, $\Theta_{\parallel a} = -\int m_a v_\parallel^2 L_1^{(3/2)} f_{a1} d\vec{v}$, and $\Theta_{\perp a} = -\int \tfrac{1}{2} m_a v_\perp^2 L_1^{(3/2)} f_{a1} d\vec{v}$.

To first order in the gyroradius expansion, the viscosity tensor has the Chew-Goldberger-Low form[42]

$$\bar{\pi}_a = (p_{\parallel a} - p_{\perp a})(\vec{n}\vec{n} - \frac{\bar{I}}{3}) ,$$

$$= p_{a0} p_a (\vec{n}\vec{n} - \frac{\bar{I}}{3}) .$$

Similarly, the "heat-viscosity tensor,"

$$\bar{\Theta}_a = -\int m_a [(\vec{v}-\vec{u}_a)(\vec{v}-\vec{u}_a) - \frac{1}{3}|\vec{v}-\vec{u}_a|^2 \bar{I}] L_1^{(3/2)}(x_a^2) f_a d\vec{v}$$

has the form

$$\bar{\Theta}_a = (\Theta_{\parallel a} - \Theta_{\perp a})(\vec{n}\vec{n} - \frac{\bar{I}}{3}) ,$$

$$= (p_{a0} p_a - \frac{7}{2} p_{a1} p_a)(\vec{n}\vec{n} - \frac{\bar{I}}{3}) .$$

The $L_j^{(1/2)}$ moments of Eq. 3-11 for $\ell=0$ give various steady-state parallel continuity equations (e.g., for density and energy) in the presence of the $\vec{E}\times\vec{B}$ drift and the diamagnetic particle and heat flows. These equations, as shown in section 3.3.2, fix the spatial variation (but not the value) of $u_{\parallel a}$ and $q_{\parallel a}$, as was done in section 3.1 for the parallel current $j_\parallel \propto u_{i\parallel} - u_{e\parallel}$.

The $L_j^{(3/2)}$ moments of Eq. 3-11 for $\ell=1$ give the steady-state parallel flux balance equations (e.g., for momentum and heat). These equations will determine the flow values, provided the other force terms (viscosities) can be calculated from higher order equations. We proceed by explicitly forming the first two flux balance equations. Taking the $\langle B\int m_a v P_1 L_0^{(3/2)} d\vec{v}\rangle = \langle B\int m_a v_\parallel d\vec{v}\rangle$ moment of Eq. 3-11 for $\ell=1$ yields the flux-surface-averaged steady state fluid momentum balance equation

$$\langle \vec{B}\cdot\nabla\cdot\bar{\pi}_a\rangle = \langle \vec{B}\cdot\vec{R}_a\rangle - n_a e_a \langle \vec{B}\cdot\vec{E}\rangle . \qquad (3\text{-}15)$$

after using

$$\langle \vec{B}\cdot\nabla\cdot\bar{\pi}_a\rangle = \langle (p_{\perp a} - p_{\parallel a})(\vec{n}\cdot\nabla B)\rangle . \qquad (3\text{-}16)$$

Note that Eq. 3-15 is the generalization of Eq. 3-3, and could, just as easily, have been obtained from single species fluid momentum balance equation (e.g., Eq. 3-2) as was done in section 3.2. Taking the $\langle B\int m_a v P_1 L_1^{(3/2)} d\vec{v}\rangle = \langle B\int m_a v_\parallel (\frac{5}{2} - \frac{v_z}{v_{Ta}^2})\rangle$ moment of the $\ell=1$ equation gives the flux-surface-averaged steady state fluid heat flux balance equation

$$\langle \vec{B}\cdot\nabla\cdot\bar{\Theta}_a\rangle = \langle \vec{B}\cdot\vec{R}_a\rangle , \qquad (3\text{-}17)$$

where $\vec{R}_a = -\int m_a \vec{v} L_1^{(3/2)} C_a(f_a, f_b) d\vec{v}$ is the heat flux friction force, and we have used

$$\langle \vec{B}\cdot\nabla\cdot\bar{\Theta}_a\rangle = \langle (\Theta_{\perp a} - \Theta_{\parallel a})(\vec{n}\cdot\nabla B)\rangle . \qquad (3\text{-}18)$$

Again, Eq. 3-17 can be obtained[15] by taking $\langle \vec{B}\cdot\ \rangle$ of the fluid heat-flow-balance equation (the $v^2\vec{v}$ moment of the Vlasov equation).

The heat-flux-balance equation must be considered because an accurate representation of the forces $\langle \vec{B}\cdot\vec{R}_a\rangle$ and $\langle \vec{B}\cdot\nabla\cdot\bar{\pi}_a\rangle$ will include terms proportional to $q_{\parallel a}$. If a more accurate representation of these forces were needed, terms proportional to higher order flows (e.g., u_{a2}) would appear, and higher order flux-balance equations would need to be considered (e.g., the $\langle B\int m_a v P_1 L_2^{(3/2)} d\vec{v}\rangle$ moment of the $\ell=1$ equation).

Now, in order to obtain equations that can be solved for the $u_{\parallel a}$, we proceed to calculate the coefficients relating the fluid forces $\langle \vec{B}\cdot\vec{R}_a\rangle$.

$\langle \vec{B}\cdot\vec{\Pi}_a \rangle$, $\langle \vec{B}\cdot\nabla\cdot\vec{\pi}_a \rangle$, and $\langle \vec{B}\cdot\nabla\cdot\vec{\Theta}_a \rangle$ to the fluid flows $u_{\parallel a}$ and $q_{\parallel a}$.

3.3.1. Friction Coefficients

The parallel friction forces are proportional to the $P_1 L_j^{(3/2)}$ moments of the collision operator, for $j = 0,1$. Since the Legendre polynomials are eigenfunctions of the collision operator, these forces may be written as

$$\vec{n}\cdot\vec{R}_a = m_a v_{Ta} \int x_a P_1^2 C_a^{(1)}(A_{a1}, A_{b1}) d\vec{v} .$$
$$\vec{n}\cdot\vec{\Pi}_a = -m_a v_{Ta} \int x_a P_1^2 L_1^{(3/2)} C_a^{(1)}(A_{a1}, A_{b1}) d\vec{v} .$$

and will thus be proportional to the $l=1$ moments of the f_{a1}, the fluid flows. Substituting the expansion for A_{a1}, Eq. 3-12, into the collision operator gives an expansion for the friction forces in terms of $l=1$ matrix elements of the collision operator

$$\vec{n}\cdot\vec{R}_a = n_a m_a \sum_b \tau_{ab}^{-1} \sum_j (u_{aj} M_{ab}^{0j} + u_{bj} N_{ab}^{0j}) \qquad (3\text{-}19)$$
$$\vec{n}\cdot\vec{\Pi}_a = -n_a m_a \sum_b \tau_{ab}^{-1} \sum_j (u_{aj} M_{ab}^{1j} + u_{bj} N_{ab}^{1j})$$

where the Braginskii Coulomb collision time[3] is

$$\tau_{ab} = \frac{3}{16\sqrt{\pi}} \frac{m_a^2 v_{Ta}^3}{n_b e_a^2 e_b^2 \ln\Lambda} .$$

$\ln\Lambda$ is the Coulomb logarithm, and the matrix elements have the form

$$M_{ab}^{ij} = \frac{2\tau_{ab}}{n_a} \int x_a P_1 L_i^{(3/2)} C_{ab}(x_a P_1 L_j^{(3/2)} f_{a0}, f_{b0}) d\vec{v} .$$
$$N_{ab}^{ij} = \frac{2\tau_{ab}}{n_a} \frac{v_{Ta}}{v_{Tb}} \int x_a P_1 L_i^{(3/2)} C_{ab}(f_{a0}, x_b P_1 L_j^{(3/2)} f_{b0}) d\vec{v} .$$

The matrix elements are evaluated in Reference (15). The symmetries of the matrix coefficients, $M_{ab}^{ij} = M_{ab}^{ji}$ and $T_b^2 v_{Tb} N_{ab}^{ij} = T_a^2 v_{Ta} N_{ba}^{ji}$ are due to the self-adjointness of the Coulomb collision operator, and lead to symmetry

relations for the friction coefficients. The friction forces, from Eq. 3-19, then become[43]

$$\vec{n}\cdot\vec{R}_e = -\vec{n}\cdot\vec{R}_i \qquad (3\text{-}20)$$
$$= l_{11}^e (u_{\parallel i} - u_{\parallel e}) + l_{12}^e \frac{2}{5} \frac{q_{\parallel e}}{p_e} ,$$
$$\vec{n}\cdot\vec{\Pi}_e = -l_{21}^e (u_{\parallel i} - u_{\parallel e}) - l_{22}^e \frac{2}{5} \frac{q_{\parallel e}}{p_e} ,$$
$$\vec{n}\cdot\vec{\Pi}_i = -l_{22}^i \frac{2}{5} \frac{q_{\parallel i}}{p_i} ,$$

where terms of relative order m_e/m_i have been eliminated. The expansions in Eq. 3-19 have been truncated at two terms, in contrast to reference (15), because the literature has not stabilized in its treatment of the next order term (proportional to u_{a2}), especially in the viscosities, and because additional terms are not expected to significantly alter the predictions for the experiment (see section 3.4). The friction coefficients are

$$l_{11}^e = \frac{n_e m_e}{\tau_{ei}}$$
$$l_{12}^e = l_{21}^e = \frac{3}{2} \frac{n_e m_e}{\tau_{ei}}$$
$$l_{22}^{ee} = (\frac{13}{4} + \sqrt{2}) \frac{n_e m_e}{\tau_{ei}}$$
$$l_{22}^i = \sqrt{2} \frac{n_i m_i}{\tau_{ii}}$$

The use of a linearized collision operator guarantees that, to $O(\delta)$, the friction coefficients are independent of collisionality regime (in contrast to the viscosities, below).

3.3.2. Viscosity Coefficients

The goal now is to solve Eq. 3-11, for $l \neq 1$, to get expressions for the viscous forces ($l=2$ moments of f_a) in terms of the flows ($l=1$ moments of f_a) that may be substituted into the flux balance equations, Eq. 3-15 and Eq. 3-17 (moments of Eq. 3-11, $l=1$). The *form* of the relation between the viscosities and the first two flows ($u_{\|a}$ and $q_{\|a}$) may be deduced from the expanded $l=0$ and $l=2$ equations after substituting

$$f_{a0}' = f_{a0}\left[\frac{p_a'}{p_a} - L_1^{(3/2)}\frac{T_a'}{T_a} + \frac{e_a\Phi'}{T_a}\right]. \tag{3-21}$$

The $L_0^{(1/2)}$ and $L_1^{(1/2)}$ moments of the $l=0$ equation then give (recalling that the collision operator conserves particles and energy)

$$0 = \vec{n}\cdot\nabla u_{\|a} - \vec{n}\cdot\nabla\frac{B}{B}u_{\|a} + 2FT_a\frac{\vec{n}\cdot\nabla B}{e_aB^2}\left[\frac{p_a'}{p_a} + \frac{e_a\Phi'}{T_a}\right],$$

$$0 = \vec{n}\cdot\nabla q_{\|a} - \vec{n}\cdot\nabla\frac{B}{B}q_{\|a} + 5FT_ap_a\frac{\vec{n}\cdot\nabla B}{e_aB^2}\left[\frac{p_a'}{p_a} + \frac{e_a\Phi'}{T_a}\right],$$

which have the solutions

$$u_{\|a} = u_{\vartheta a}B + F\frac{T_a}{e_aB}\left[\frac{p_a'}{p_a} + \frac{e_a\Phi'}{T_a}\right], \tag{3-22}$$

$$q_{\|a} = q_{\vartheta a}B + \frac{5}{2}Fp_a\frac{T_a}{e_aB}\left[\frac{T_a'}{T_a}\right],$$

where $u_{\vartheta a}$ and $q_{\vartheta a}$ are constants of integration, and are identified as the poloidal flow velocity and poloidal heat flow, respectively. Substituting these expressions into Eq. 3-11 for $l=2$, we see that the flow velocity and heat flow only appear through terms proportional to $u_{\vartheta a}\vec{n}\cdot\nabla B$ and $q_{\vartheta a}p_a^{-1}\vec{n}\cdot\nabla B$. Since the $l=2$ equation is the only unused equation containing the $l=1$ moments of f_a, and since all the equations are linear in the moments of f_a, the ultimate solutions for the two lowest order viscosities in terms of the two lowest order flows must take the form

$$\langle\vec{B}\cdot\nabla\cdot\vec{\pi}_a\rangle = 3\langle(\vec{n}\cdot\nabla B)^2\rangle\sum_b\left(\mu_{11}^{ab}u_{\vartheta b} + \mu_{12}^{ab}\frac{2}{5}\frac{q_{\vartheta b}}{p_b}\right), \tag{3-23}$$

$$\langle\vec{B}\cdot\nabla\cdot\vec{\Theta}_a\rangle = 3\langle(\vec{n}\cdot\nabla B)^2\rangle\sum_b\left(\mu_{21}^{ab}u_{\vartheta b} + \mu_{22}^{ab}\frac{2}{5}\frac{q_{\vartheta b}}{p_b}\right),$$

where the μ_{ij}^{ab} are the collisionality-dependent viscosity coefficients, and the overall factor of three is inserted[43] so that μ_{11}^{aa} reduces to the classical value in the collisional limit. Thus, as discussed in section 3.2, the viscous forces depend only on the poloidal flows, and act to damp them out. The inter-species couplings in Eq. 3-23 arise from the field-particle terms (second term in Eq. 3-9) of the linearized collision operator in Eq. 3-11 for $l \geq 2$. Since the test-particle terms (first term in Eq. 3-9) typically dominate the field-particle terms[41] by a factor of l^2, the inter-species coupling terms in Eq. 3-23 will be dropped.

Unfortunately, the system of equations Eq. 3-11, for $l \geq 2$, cannot be solved analytically for the viscosity coefficients at all collision frequencies. The standard technique is to obtain analytic solutions in several asymptotic collisionality regimes, and smooth these together to obtain uniformly applicable expressions. These regimes are: (1) The collisional (or fluid) regime, when the collision operator is dominant and trapped particle effects are ignorable. This occurs for $\tau_a < \tau_{aB}$, where τ_{aB} is the thermal bounce frequency. (2) The collisionless (or banana) regime,

when trapped particle effects dominate and particle are assumed to complete many ("banana") drift orbits before suffering a detrapping collision. This occurs for $\tau_a > \tau_{aB}/f_t$, where f_t is the trapped particle fraction. (3) The intermediate (or plateau) regime, when $\tau_a \gtrsim \tau_{aB}$, and thus resonant particles do not have their cross-flux-surface drift $(\vartheta_{Da}\cdot\nabla\psi)$ canceled before scattering.

3.3.2.1. Fluid (Collisional) Regime

The collisional viscosity has been calculated by several different methods.[44,45] The expression used is Eq. 3-11 $l=2$, where the $l=3$ moments of f_{a1} are taken to be of order $\frac{\tau_{aa}}{\tau_{aB}} \ll 1$ relative to the rest of the terms, and neglected. Expanding A_{a1} and A_{a2} using Eqs. 3-12 and 3-14, truncating both expansions after the first two terms, and using Eq. 3-22 gives

$$2x_a^2\left[u_{\vartheta a}L_0^{(3/2)} + \frac{2}{5}\frac{q_{\vartheta a}}{p_a}L_1^{(3/2)}\right](\hat{n}\cdot\nabla B)P_2 f_{a0} ,$$
$$= \sum_b C_{ab}\left(\frac{2}{3}x_a^2(p_{a0}+p_{a1})P_2 f_{a0}, f_{b0}\right)$$

where the field-particle terms have been neglected in the collision operator. Taking the $x^2L_0^{(5/2)}P_2$ and $x^2L_1^{(5/2)}P_2$ moments gives the coupled equations

$$\frac{3}{2}n_a\left(u_{\vartheta a} - \frac{2}{5}\frac{q_{\vartheta a}}{p_a}\right)$$
$$= \sum_{j=0}^{1} p_{aj}\sum_b \int x_a^4 L_0^{(5/2)}P_2\, C_{ab}\left(\frac{2}{3}x_a^2 L_j^{(5/2)}P_2 f_{a0}, f_{b0}\right) d\vec{v} .$$

$$\frac{21}{4}n_a\frac{2}{5}\frac{q_{\vartheta a}}{p_a}$$
$$= \sum_{j=0}^{1} p_{aj}\sum_b \int x_a^4 L_1^{(5/2)}P_2\, C_{ab}\left(\frac{2}{3}x_a^2 L_j^{(5/2)}P_2 f_{a0}, f_{b0}\right) d\vec{v} .$$

The matrix elements of the collision operator are given, and the equations inverted, in Reference (15). For a simple (Hydrogen) plasma, the viscosity coefficients are then evaluated to be:

$$\mu_{11}^{ee} = \frac{n_e m_e}{\tau_{ee}}\lambda_{ee}^2\frac{0.731}{2}, \qquad (3\text{-}24)$$
$$\mu_{12}^{ee} = \mu_{21}^{ee} = \frac{n_e m_e}{\tau_{ee}}\lambda_{ee}^2\frac{3.273}{2},$$
$$\mu_{22}^{ee} = \frac{n_e m_e}{\tau_{ee}}\lambda_{ee}^2\frac{16.059}{2}.$$

$$\mu_{11}^{ii} = \frac{n_i m_i}{\tau_{ii}}\lambda_{ii}^2\frac{1.358}{2},$$
$$\mu_{12}^{ii} = \mu_{21}^{ii} = \frac{n_i m_i}{\tau_{ii}}\lambda_{ii}^2\frac{5.586}{2},$$
$$\mu_{22}^{ii} = \frac{n_i m_i}{\tau_{ii}}\lambda_{ii}^2\frac{26.363}{2},$$

where $\lambda_{aa} = v_{Ta}\tau_{aa}$ is the mean free path, and terms of order $(m_e/m_i)^{\frac{1}{2}}$ have been omitted.

3.3.2.2. Plateau (Intermediate) Regime

The plateau regime viscosity coefficients have been calculated directly, for large aspect ratio and circular cross section, by Shaing and Callen.[46] They have also been indirectly calculated[47] by comparing the calculated cross-flux-surface particle and heat flux with expressions for these fluxes in terms of the parallel viscosities. In either case, the plateau calculations assume $\delta_B \ll 1$, and thus $f_t \ll 1$, where $\delta_B = (B_{Max} - B_{Min})/(B_{Max} + B_{Min})$ is the magnetic field modulation parameter, and B_{Max} and B_{Min} are the magnetic field strength maxima and minima for a given flux surface.

The direct calculation proceeds by noticing that the standard solution[48] to the first order DKE (Eq. 3-8), in the plateau regime, has the form[46]

$$f_{a1} = P_1(\frac{v_\parallel}{v}) \left[S_a(\psi,v) \frac{B}{<B^2>^{1/2}} f_{a0} + F \frac{v}{\Omega_a} f'_{a0} \right] + h_{a1} , \qquad (3\text{-}25)$$

where h_{a1} is the "localized" portion of the distribution function, and is of order $(\tau_{aB}/\tau_a)^{-1/3}\delta_B \ll 1$ with respect to first term.[48] Therefore, the portion in square brackets is taken as equal to A_{a1}, and expanded in Laguerre polynomials using Eq. 3-12, giving

$$S_a(\psi,v) = \frac{2\pi_a}{v_{Ta}} \left[u_{\phi a} - \frac{2}{5} \frac{q_{\phi a}}{p_a} \right] <B^2>^{1/2}$$

where the expansion has been truncated after the first two terms. Eq. 3-25 is substituted into the DKE, Eq. 3-8, which is solved for h_{a1} in terms of S_a, and thus $u_{\phi a}$ and $q_{\phi a}$. The viscosity coefficients are obtained by

directly integrating h_{a1} to evaluate Eqs. 3-16 and 3-18 (the rest of f_{a1} does not contribute, as it is proportional to P_1), giving[46]

$$\mu_{aa}^{11} = \frac{n_a m_a}{\tau_{aa}} \lambda_{aa} L_c \frac{\sqrt{\pi}}{6} \Gamma(3) , \qquad (3\text{-}26)$$

$$\mu_{aa}^{12} = \frac{n_a m_a}{\tau_{aa}} \lambda_{aa} L_c \frac{\sqrt{\pi}}{6} [\Gamma(4) - \frac{5}{2}\Gamma(3)] ,$$

$$\mu_{aa}^{12} = \frac{n_a m_a}{\tau_{aa}} \lambda_{aa} L_c \frac{\sqrt{\pi}}{6} [\Gamma(5) - 5\Gamma(4) + \frac{25}{4}\Gamma(3)] ,$$

where $L_c^2 = <B^2> / <(\vec{n}\cdot\nabla B)^2>$ is the connection length.

The indirect calculation of the viscosity coefficients [47, 15] includes the effect of non-circular flux surface cross section (but is still restricted to $\delta_B \ll 1$). The net effect of the more general cross section is to replace L_c in the above expressions for μ_{ij}^{aa} with the "effective" connection length

$$L_c^* = \frac{<B^2>^2}{<(\vec{n}\cdot\nabla B)^2><\vec{B}\cdot\nabla\vartheta>} \sum_k \frac{2}{k} \left[<\frac{\vec{n}\cdot\nabla B}{B} \sin k\Theta> <\frac{\vec{n}\cdot\nabla B}{B^2} \sin k\Theta> \right] ,$$

where ϑ is the poloidal angle, and

$$\Theta(\vartheta) = 2\pi \frac{\int_0^\vartheta \frac{d\hat{\vartheta}}{\vec{n}\cdot\nabla\hat{\vartheta}}}{\int_0^{2\pi} \frac{d\hat{\vartheta}}{\vec{n}\cdot\nabla\hat{\vartheta}}} .$$

3.3.2.3. Banana (Collisionless) Regime

In the collisionless regime, thermal trapped particles complete several bounce orbits before suffering a detrapping collision. This implies that $\nu_{*a} < 1$[2, 15] where

$$\nu_{*a} \equiv \frac{L_c}{v_{Ta}\tau_a} \delta_B^{3/2} .$$

In order to compute the viscosity, ν_{ta} is taken as an expansion parameter for Eq. 3-8 and f_{a1}. The lowest order (ν_{ta}^0) equation

$$v\,\vec{n}\cdot\nabla\left(f_{a1}^{(0)} - F(\psi)f_{a0}'\frac{v_\parallel}{\Omega_a}\right) = 0\,,$$

where $f_{a1} = f_{a1}^{(0)} + f_{a1}^{(1)} + \cdots$, gives the form of the lowest order solution[49]

$$f_{a1}^{(0)} = F\,\frac{v_\parallel}{\Omega_a}f_{a0}' + g_a(v, v_\parallel, \psi)\,, \tag{3-27}$$

where g_a is an integration constant, to be determined. The next order ($\nu\frac{i}{ta}$) equation is

$$v\,\vec{n}\cdot\nabla f_{a1}^{(1)} - v_\parallel\frac{e_a E_\parallel}{T_a} = C_a(f_{a1}^{(0)}, f_{b1}^{(0)})\,. \tag{3-28}$$

Integrating over a bounce orbit (for both trapped and circulating particles) gives constraint equations for g_a. For circulating particles, taking $\langle B/v_\parallel\rangle$ of Eq. 3-28 gives

$$-\frac{e_a}{T_a}\langle\vec{B}\cdot\vec{E}\rangle = \left\langle\frac{B}{v_\parallel}C_a(f_{a1}^{(0)}, f_{b1}^{(0)})\right\rangle\,. \tag{3-29a}$$

The solution to this equation has the form[49,50]

$$g_a = \frac{2V_\parallel(\lambda,v)\,C_a(v)}{v^2 f_a}f_{a0}\,,$$

where $\lambda\equiv v_\perp^2/(Bv^2)$ is the pitch angle, and

$$V_\parallel(\lambda,v) = \frac{v^2}{2}\langle B^2\rangle^{\frac{1}{2}}\int_\lambda^{\lambda_c}\frac{d\lambda'}{\langle v_\parallel(\lambda')\rangle}\,.$$

For trapped particles, integrating Eq. 3-28 over a closed "banana" orbit gives

$$0 = \int\frac{dl_\parallel}{v_\parallel}C_a(g_a, g_b)\,. \tag{3-29b}$$

which implies $g_a = 0$. Substituting these forms for g_a into Eq. 3-27, and taking $v_\parallel L_j^{(3/2)}$ moments of both sides, gives an expansion for g_a

$$g_a = \frac{2V_\parallel H(\lambda_c-\lambda)}{v_{Ta}^2}\frac{\langle B^2\rangle^{\frac{1}{2}}}{f_c}\left[u_{\phi a} - \frac{2}{5}\frac{q_{\phi a}}{p_a}L_1^{(3/2)}(x_a^2)\right]\,, \tag{3-30}$$

where the expansion has been truncated after the first two terms. H is the Heaviside step function, $\lambda_c = B_{MAX}^{-1}$ is the largest pitch angle for circulating particles,

$$f_c = \langle B^2\rangle\frac{3}{4}\int_0^{\lambda_c}\frac{\lambda'\,d\lambda'}{\langle v_\parallel(\lambda')\rangle}$$

is the fraction of circulating particles, $f_t = 1 - f_c$. Hirshman and Sigmar[15] then substitute this expression for g_a into Eq. 3-28, and using Eq. 3-29a obtain

$$v_\parallel\vec{n}\cdot\nabla f_{a1}^{(1)} = C_a(g_a, f_{b0}) - \frac{V_\parallel H(\lambda_c-\lambda)}{f_c}\frac{\langle B^2\rangle^{\frac{1}{2}}}{B^2}\left\langle\frac{B}{v_\parallel}C_a(g_a, f_{b0})\right\rangle\,.$$

Taking $v_\parallel L_j^{(3/2)}$ moments of this equation gives relations (like Eq. 3-12 for $l=1$) between $u_{\phi a}$, $q_{\phi a}$, and the viscous forces. They solve these to obtain (for a simple Hydrogen plasma):

$$\mu_{11}^{ee} = \frac{n_e m_e}{\tau_{ee}}L_c^2\frac{f_t}{f_c}\frac{1}{3}\left[\sqrt{2} - \ln(1+\sqrt{2}) + 1\right]\,, \tag{3-31}$$

$$\mu_{12}^{ee} = \frac{n_e m_e}{\tau_{ee}}L_c^2\frac{f_t}{f_c}\frac{1}{3}\left[-\frac{4}{\sqrt{2}} + \frac{5}{2}\ln(1+\sqrt{2}) - \frac{3}{2}\right]\,,$$

$$\mu_{22}^{ee} = \frac{n_e m_e}{\tau_{ee}}L_c^2\frac{f_t}{f_c}\frac{1}{3}\left[\frac{39}{4\sqrt{2}} - \frac{25}{4}\ln(1+\sqrt{2}) + \frac{13}{4}\right]\,,$$

$$\mu_{11}^{ii} = \frac{n_i m_i}{\tau_{ii}}L_c^2\frac{f_t}{f_c}\frac{1}{3}\left[\sqrt{2} - \ln(1+\sqrt{2})\right]\,,$$

$$\mu_{12}^{ii} = \frac{n_i m_i}{\tau_{ii}}L_c^2\frac{f_t}{f_c}\frac{1}{3}\left[-\frac{4}{\sqrt{2}} + \frac{5}{2}\ln(1+\sqrt{2})\right]\,,$$

$$\mu_{22}^{\alpha} = \frac{n_i m_i}{\tau_{\alpha}} L_c^2 \frac{f_t}{f_c} \frac{1}{3} \left[\frac{39}{4\sqrt{2}} - \frac{25}{4} \ln(1+\sqrt{2}) \right],$$

where terms of order $(m_e/m_i)^{1/2}$ have been dropped.

3.3.2.4. Viscosity Coefficient Smoothing

The viscosity coefficients derived above are only valid in the appropriate asymptotic collisionality regime. Approximate coefficients, for arbitrary thermal collision frequency, may be obtained[51,48,15] by piecing together the asymptotic solutions for f_{a1}, using each asymptotic solution for those portions of the approximate f_{a1} where the local (in v) collision frequency obeys the appropriate constraints (see section 3.3). For instance, using Eq. 3-16, the approximate parallel viscous force is

$$\langle \vec{B}\cdot\nabla\cdot\vec{\pi}_a \rangle = -\langle 2T_a(\vec{n}\cdot\nabla B)\left[\int_0^{v_P} x_a^2 L_0^{(5/2)} P_2 f_{a1}^{PS}\, d\vec{v} \right. \tag{3-32}$$

$$\left. + \int_{v_P}^{v_B} x_a^2 L_0^{(5/2)} P_2 f_{a1}^{P}\, d\vec{v} + \int_{v_B}^{\infty} x_a^2 L_0^{(5/2)} P_2 f_{a1}^{B}\, d\vec{v} \right] \rangle ,$$

where f_{a1}^{PS}, f_{a1}^{P}, f_{a1}^{B} are the perturbed distribution functions in the Pfirsch-Schlüter, plateau, and banana regimes, respectivly, $v_P(v_{Ta})$ is the velocity-boundary between the Pfirsch-Schlüter and plateau regime portions of f_a, and $v_B(v_{Ta})$ is the velocity-boundary between plateau and banana regimes. Such a partition of the distribution function is only reasonable to the extent that pitch-angle scattering dominates the rest of the collision operator, and thus the different energy sections of f_a are not coupled through C_a (and thus are not coupled in the DKE).

Rather than evaluate Eq. 3-32, and its analogue for $\langle \vec{B}\cdot\nabla\cdot\vec{\Theta}_a \rangle$, Hirshman and Sigmar provide, ad hoc, two methods to directly smooth the viscosity coefficients.[15] These have the advantage of preserving the symmetry $\mu_{12}^{\alpha\alpha}=\mu_{21}^{\alpha\alpha}$ which is generally destroyed in equations of the form of Eq. 3-32. Their "more exact method" is applicable only to small magnetic modulation geometries ($\delta_B \ll 1$), and is obtained by "identifying"[48] a form for the viscosity coefficients that give the appropriate asymptotic values in the asymptotic limits. It uses a smoothed collision frequency, obtained from a simple rational combination (as in Eq. 3-34, below) of effective collision frequencies for each regime.

The other method, employed here, approximates each viscosity coefficient by a rational combination of the asymptotic coefficients, giving a smooth transition from one regime to another. Since some of the coeffients change sign from one regime to another (e.g., $\mu_{12}^{\alpha\alpha}$), a positive-definite viscosity coefficient matrix[15] must be employed,

$$\begin{aligned} K_{11}^{\alpha} &= \mu_{11}^{\alpha\alpha}, \\ K_{12}^{\alpha} &= \mu_{12}^{\alpha\alpha} + \frac{5}{2}\mu_{11}^{\alpha\alpha}, \\ K_{22}^{\alpha} &= \mu_{22}^{\alpha\alpha} + 5\mu_{12}^{\alpha\alpha} + \frac{25}{4}\mu_{11}^{\alpha\alpha}. \end{aligned} \tag{3-33}$$

Using this matrix, the smoothed form is[15]

$$K_{ij}^{\alpha}(v_{Ta}) = \frac{K_{ij}^{\alpha PS} K_{ij}^{\alpha P} K_{ij}^{\alpha B}}{\left[K_{ij}^{\alpha PS} + K_{ij}^{\alpha P} \right]\left[K_{ij}^{\alpha P} + K_{ij}^{\alpha B} \right]}, \tag{3-34}$$

where $K_{ij}^{\alpha PS}(v_{Ta})$, $K_{ij}^{\alpha P}(v_{Ta})$, and $K_{ij}^{\alpha B}(v_{Ta})$ are the coefficient evaluated as if in the asymptotic Pfirsch-Schlüter, plateau, and banana regimes, respec-

tively.

3.3.3. Calculation of Currents

Substituting Eqs. 3-20, 3-22, and 3-23 into the flux surface averaged flux balance equations,Eqs. 3-15 and 3-17, gives the coupled equations

$$3\langle(\vec{n}\cdot\nabla B)^2\rangle\,(\mu_{11}^{ee}u_{\vartheta e}+\mu_{12}^{ee}\frac{2}{5}\frac{q_{\vartheta e}}{p_e}) \qquad (3\text{-}35)$$
$$= l_{11}^{e}\left[(u_{\vartheta i}-u_{\vartheta e})\langle B^2\rangle-\frac{F}{eB}(\frac{p_i'}{n_i}+\frac{p_e'}{n_e})\right]$$
$$+\,l_{12}^{e}\left[\frac{2}{5}\frac{q_{\vartheta e}}{p_e}+\frac{F}{eB}T_e'\right]-n_e e\langle\vec{B}\cdot\vec{E}\rangle\,,$$

$$3\langle(\vec{n}\cdot\nabla B)^2\rangle\,(\mu_{11}^{ii}u_{\vartheta i}+\mu_{12}^{ii}\frac{2}{5}\frac{q_{\vartheta i}}{p_i})$$
$$= -l_{11}^{e}\left[(u_{\vartheta i}-u_{\vartheta e})\langle B^2\rangle-\frac{F}{eB}(\frac{p_i'}{n_i}+\frac{p_e'}{n_e})\right]$$
$$-\,l_{12}^{e}\left[\frac{2}{5}\frac{q_{\vartheta e}}{p_e}+\frac{F}{eB}T_e'\right]+n_i e\langle\vec{B}\cdot\vec{E}\rangle\,,$$

$$3\langle(\vec{n}\cdot\nabla B)^2\rangle\,(\mu_{21}^{ee}u_{\vartheta e}+\mu_{22}^{ee}\frac{2}{5}\frac{q_{\vartheta e}}{p_e})$$
$$= -l_{21}^{e}\left[(u_{\vartheta i}-u_{\vartheta e})\langle B^2\rangle-\frac{F}{eB}(\frac{p_i'}{n_i}+\frac{p_e'}{n_e})\right]$$
$$-\,l_{22}^{e}\left[\frac{2}{5}\frac{q_{\vartheta e}}{p_e}+\frac{F}{eB}T_e'\right],$$

$$3\langle(\vec{n}\cdot\nabla B)^2\rangle\,(\mu_{21}^{ii}u_{\vartheta i}+\mu_{22}^{ii}\frac{2}{5}\frac{q_{\vartheta i}}{p_i}) = -l_{22}^{e}\left[\frac{2}{5}\frac{q_{\vartheta i}}{p_i}-\frac{F}{eB}T_i'\right],$$

where the field particle terms have been ignored in the expression for the viscosities, and terms of order $(m_e/m_i)^{1/2}$ have been neglected in the friction forces. Thus, we are left with four linear equations in four unknowns ($u_{\vartheta i}$, $q_{\vartheta i}$, $u_{\vartheta e}$, and $q_{\vartheta e}$). These are inverted (best by a computer, e.g., SMP, Reduce, or MACSYMA) and combined with Eq. 3-1, using $n\equiv n_e\simeq n_i$ and $K(\psi)=n\,e\,(u_{\vartheta i}-u_{\vartheta e})$, to give a direct expression for the parallel current

$$j_{\parallel}=\frac{Fp'}{B}-\frac{FBp}{\langle B^2\rangle}\left[\frac{p'}{p}(1-\hat{L}_{31})-\frac{T_e'}{T}\hat{L}_{32}-\frac{T_i'}{T}\hat{L}_{32}^{i}\right] \qquad (3\text{-}36)$$
$$+\,\sigma_{NC}\langle\vec{B}\cdot\vec{E}\rangle\,,$$

where $p\equiv p_e+p_i$, $T\equiv T_e+T_i$, and the $\hat{L}_{ij}$ are normalized transport coefficients, elements of the Onsager matrix, relating the current (flux of charge) to the various thermodynamic forces. These coefficients are given by

$$\hat{L}_{31}=\frac{\hat{\mu}_{11}^{e}(l_{22}^{e}+\hat{\mu}_{22}^{e})+\hat{\mu}_{12}^{e}(l_{12}^{e}-\hat{\mu}_{12}^{e})}{(\hat{\mu}_{11}^{e}+l_{11}^{e})(l_{22}^{e}+\hat{\mu}_{22}^{e})-(l_{12}^{e}-\hat{\mu}_{12}^{e})^2}, \qquad (3\text{-}37)$$

$$\hat{L}_{32}=\frac{\hat{\mu}_{12}^{e}(l_{22}^{e}+\hat{\mu}_{22}^{e})+\hat{\mu}_{22}^{e}(l_{12}^{e}-\hat{\mu}_{12}^{e})}{(\hat{\mu}_{11}^{e}+l_{11}^{e})(l_{22}^{e}+\hat{\mu}_{22}^{e})-(l_{12}^{e}-\hat{\mu}_{12}^{e})^2},$$

$$\hat{L}_{32}^{i}=\hat{L}_{31}\frac{l_{22}^{i}\hat{\mu}_{12}^{i}}{\hat{\mu}_{11}^{i}(l_{22}^{i}+\hat{\mu}_{22}^{i})-(\hat{\mu}_{12}^{i})^2},$$

$$\sigma_{NC}=(ne)^2\frac{l_{22}^{e}+\hat{\mu}_{22}^{e}}{(\hat{\mu}_{11}^{e}+l_{11}^{e})(l_{22}^{e}+\hat{\mu}_{22}^{e})-(l_{12}^{e}-\hat{\mu}_{12}^{e})^2},$$

where $\hat{\mu}_{ij}^{a}\equiv\mu_{ij}^{aa}\frac{3\langle(\vec{n}\cdot\nabla B)^2\rangle}{\langle B^2\rangle}$, and terms of order $(\frac{m_e}{m_i})^{1/2}\sim\frac{l_{22}^{e}}{l_{22}^{i}}\sim\frac{\mu_{jk}^{e}}{\mu_{jk}^{i}}$ have

been dropped. The ohmic-current term is often written as

$$\sigma_{NC} \langle \vec{B} \cdot \vec{E} \rangle = (\sigma_S - \hat{L}_{33}) \langle \vec{B} \cdot \vec{E} \rangle ,$$

where

$$\hat{L}_{33} = \sigma_S (\hat{L}_{31} + \frac{l^e_{12}}{l^e_{22}} \hat{L}_{32}) .$$

Note that $\hat{L}_{31} \leq 1$. In the collisional limit, $\hat{L}_{31} \to 0$ leaving the Pfirsch-Schlüter current. The terms proportional to $\hat{L}_{31}$, $\hat{L}_{32}$, and $\hat{L}^i_{32}$ are the bootstrap current.

If the cross coefficients (l^a_{12} and μ^a_{12}) coupling the heat-flows to the momentum forces ($\vec{n} \cdot \vec{R}_a$ and $\vec{n} \cdot \nabla \cdot \vec{\pi}_a$) are set to zero, decoupling the heat flows from the problem, giving

$$\hat{L}_{31} \simeq \frac{\hat{\mu}^e_{11}}{\hat{\mu}^e_{11} + l^e_{11}} , \qquad (3\text{-}38)$$
$$\hat{L}_{32} \simeq \hat{L}^i_{32} \simeq 0 .$$

These may also be obtained from Eq. 3-6 (the simplified calculation of section 3.2) using the form of the viscosity, Eq. 3-23.

The portion of the current carried by the ions is given by

$$j_{i\parallel} = (p_i' + ne\Phi') \frac{F}{B} + \sigma_{NCi} \langle \vec{B} \cdot \vec{E} \rangle \qquad (3\text{-}39)$$
$$- \frac{FBp}{\langle B^2 \rangle} \left[\frac{p'}{p} (1 - \hat{L}_{31i}) - \frac{T_e'}{T} \hat{L}^e_{32i} - \frac{T_i'}{T} \hat{L}^i_{32i} \right] ,$$

where the ion parallel transport coefficients are

$$(1 - \hat{L}_{31i}) = L_i \frac{l^e_{11} \hat{\mu}^{e\,2}_{12} + l^{e\,2}_{12} \hat{\mu}^e_{11} - l^e_{11} \hat{\mu}^e_{11} (l^e_{22} + \hat{\mu}^e_{22})}{(\hat{\mu}^e_{11} + l^e_{11})(l^e_{22} + \hat{\mu}^e_{22}) - (l^e_{12} - \hat{\mu}^e_{12})^2} , \qquad (3\text{-}40)$$

$$\hat{L}^e_{32i} = L_i \frac{l^e_{12} \hat{\mu}^{e\,2}_{12} - l^{e\,2}_{12} \hat{\mu}^e_{12} + l^e_{11} \hat{\mu}^e_{12} l^e_{22} - \hat{\mu}^e_{11} l^e_{12} \hat{\mu}^e_{22})}{(\hat{\mu}^e_{11} + l^e_{11})(l^e_{22} + \hat{\mu}^e_{22}) - (l^e_{12} - \hat{\mu}^e_{12})^2} ,$$

$$\hat{L}^i_{32i} = \frac{l^i_{22} \hat{\mu}^i_{12}}{\hat{\mu}^i_{11} (l^i_{22} + \hat{\mu}^i_{22}) - \hat{\mu}^{i\,2}_{12}} ,$$

$$\sigma_{NCi} = (ne)^2 L_i \hat{L}_{31} , \text{ and}$$

$$L_i = \frac{(l^i_{22} + \hat{\mu}^i_{22})}{\hat{\mu}^i_{11} (l^i_{22} + \hat{\mu}^i_{22}) - \hat{\mu}^{i\,2}_{12}}$$

The first term in Eq. 3-39 ensures ion continuity in the presence of the ion diamagnetic and $\vec{E} \times \vec{B}$ drifts. The ion parallel transport coefficients, excepting $\hat{L}^i_{32i}$, are seen to be smaller than the corresponding total-current parallel transport coefficients, by a factor of order $(m_e / m_i)^{1/2}$. To this order

$$j_{i\parallel} = (p_i' + ne\Phi') \frac{F}{B} + \frac{FB}{\langle B^2 \rangle} n_i T_i' \hat{L}^i_{32i} .$$

Thus, for $T_i' = 0$, $\hat{L}_{31i} \simeq 1$ and it is as if the ion bootstrap current were maximal. Comparing with Eq. 3-22, this implies that the poloidal ion flow velocity is negligible (except for the term proportional to T_i') when compared to the poloidal electron flow velocity, or the toroidal ion flow velocity. The ion poloidal velocity is suppressed, due to the large ion viscosity coefficients.[52]

3.4. Calculation of Octupole Currents

The expected parallel current level in the octupole is calculated using numeric flux plots calculated by the program SOAK[21,22] which includes the time-dependent distortion of the flux surfaces due to the finite-resistivity of the boundary conductors. The flux plots for 20 msec

and 25 msec (into the inductive magnetic field pulse) are used to compare with experiment, as these best correspond to times of experimental interest. Individual flux surfaces are interpolated from the flux plots, generating a data base for the calculation of flux surface integrals and local current levels. A comparison between calculated and experimentally measured B_P and B_T, along the $\psi = 6.5$ flux surface, is shown in Fig. 3-3.

Figs. 3-4 and 3-5 show the variation of the field modulation, δ_B, and the circulating particle fraction, f_c, across the flux surfaces for typical magnetic fields used in the experiments. The seperatrix, ψ_{Sep}, is at ψ=5.7, and the last minimum-average-B stable flux surface, ψ_{Crit}, is at ψ=8.2. Due to the very small circulating particle fraction, especially for the outer flux surfaces ($\psi > \psi_{Sep}$), the plateau regime is effectively absent (as $f_t \simeq 1$., see the discusion of the collisionality regimes in section 3.3.2). The plateau regime will not be included in the calculation for these outer flux surfaces, and thus the smoothing expression used (instead of Eq. 3-34) is

$$K_{ij}^a(\nu_{Ta}) = \frac{K_{ij}^{a\ PS}\, K_{ij}^{a\ B}}{K_{ij}^{a\ PS} + K_{ij}^{a\ B}}. \qquad (3\text{-}41)$$

Fig. 3-6 shows the computed dependence of $(1 - \hat{L}_{31})$ on λ_{ee} for $\psi = 6.5$, from Eq. 3-37. Included are curves calculated using the asymptotic viscosity coefficients for the fluid and banana regimes, as well as the smoothed coefficients. If the heat flows are neglected in the calculation

of $j_{\|}$, and thus Eq. 3-38 used to calculate $(1 - \hat{L}_{31})$, Fig. 3-7 results. Note that the inclusion of the heat flows does not significantly alter the collisionality dependence of the currents. Thus, it is not expected that terms related to the next order flow (u_{a2}) would contribute significantly to the calculation. This justifies the truncation of all Laguerre polynomial expansions after two terms.

The relatively weak variations of $(1 - \hat{L}_{31})$ with B_T and ψ are shown in Figs. 3-8 and 3-9. Almost all of the expected variation of $j_{\|}$ with B_T is thus due to the overall factor of $F = R\,B_T$ in Eq. 3-39.

The fraction of poloidal current carried by the ions (due to p') is shown in Fig. 3-10. As expected, due to the high ion viscosity, the ions carry almost none of the poloidal current, and basically do not rotate poloidaly. Note that this holds true even as $\lambda \to p$, where this theoretical treatment becomes invalid. Figs. 3-11 and 3-12 show the variation of $\hat{L}_{32}^{e}$ and $\hat{L}_{32}^{i}$ (coefficients coupling the parallel current to the perpendicular temperature gradients) with λ_{ee}. For the plasmas studied, typically $\frac{p'}{p} \gg \frac{T_e'}{T} \simeq \frac{T_i'}{T}$ (see section 2.4). Thus these coefficients are usually not important for this experiment.

Fig. 3-1. Coordinate system used. $\hat{\varphi}$ and $\hat{\chi}$ are tangent to the flux surface, in the toroidal and poloidal directions, respectively. $\hat{\psi}$ is perpendicular to the flux surface.

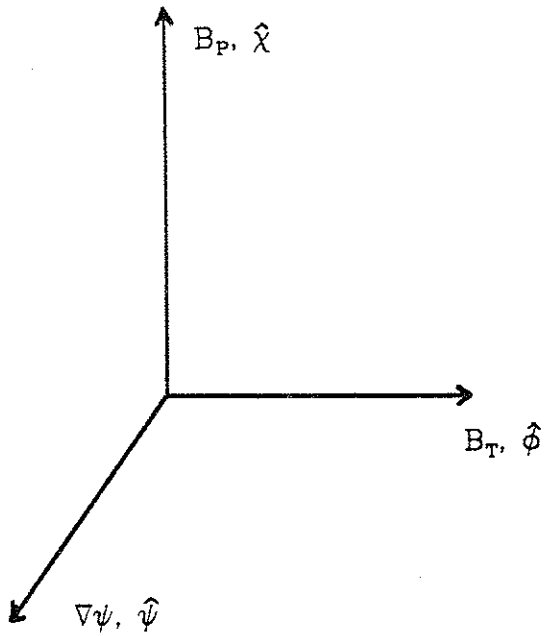

Fig. 3-2. When the neoclassical viscosity is large, the plasma generates whatever parallel current necessary so that the total current is toroidal.

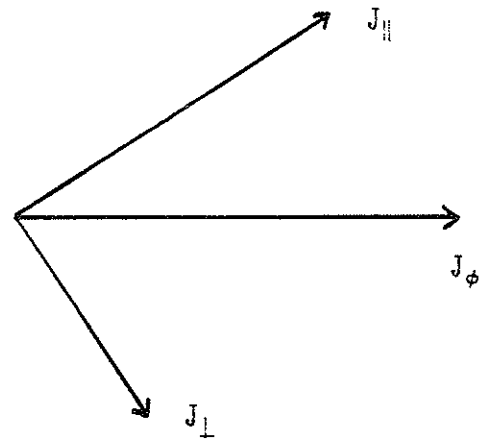

Fig. 3-3. Measured (points) and calculated (curve) B_P for around $\psi = 7.0$.

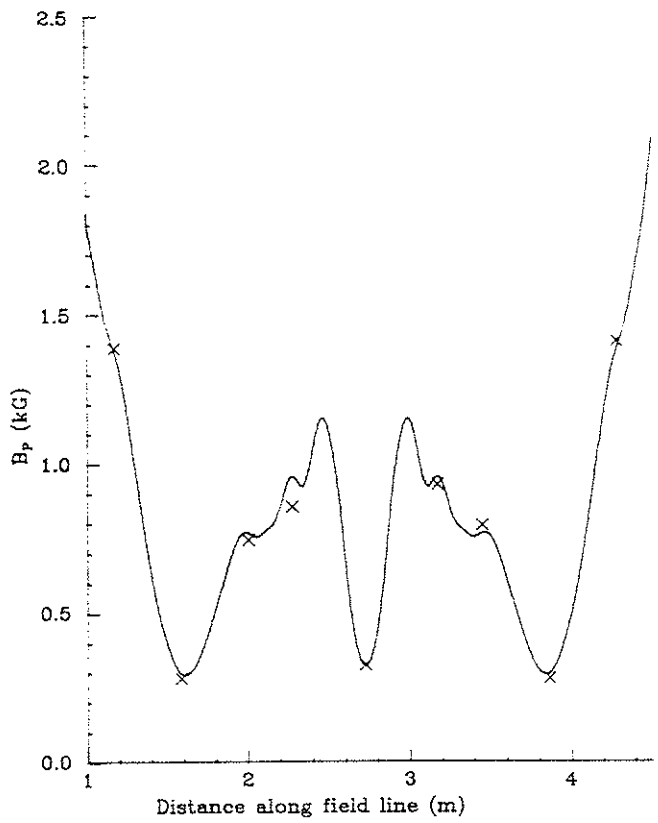

Fig. 3-4. Profile of δ_B, the magnetic modulation, for $B_T = 400\ G$ on axis. The dotted curve is for the inner flux surfaces of the inner hoops.

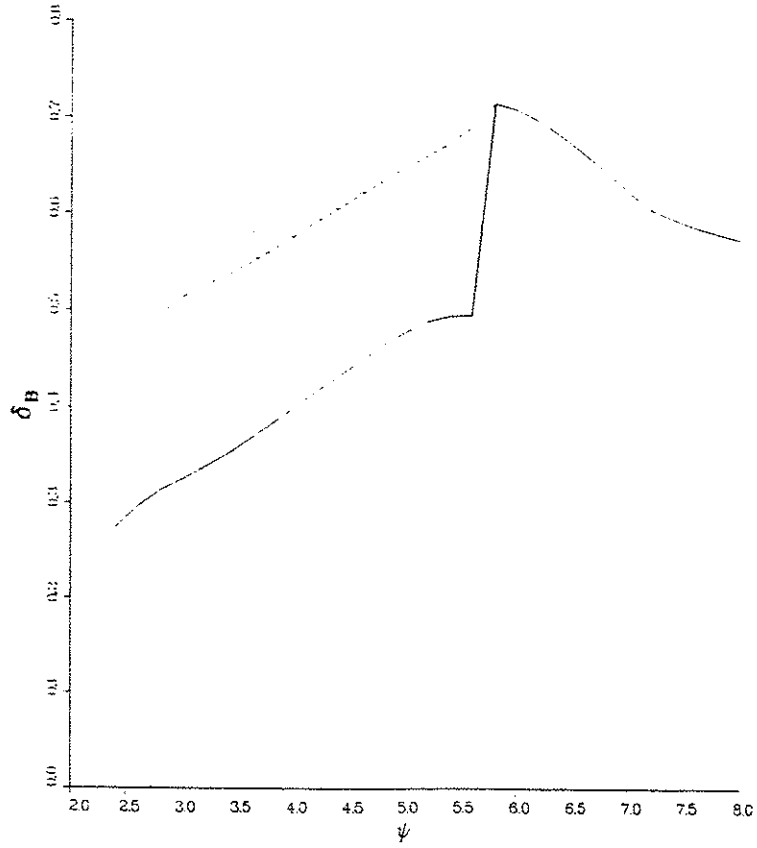

Fig. 3-5. Profile of f_c, the circulating particle fraction, for $B_T = 400$ G on axis. The dotted curve is for the inner flux surfaces of the inner hoops.

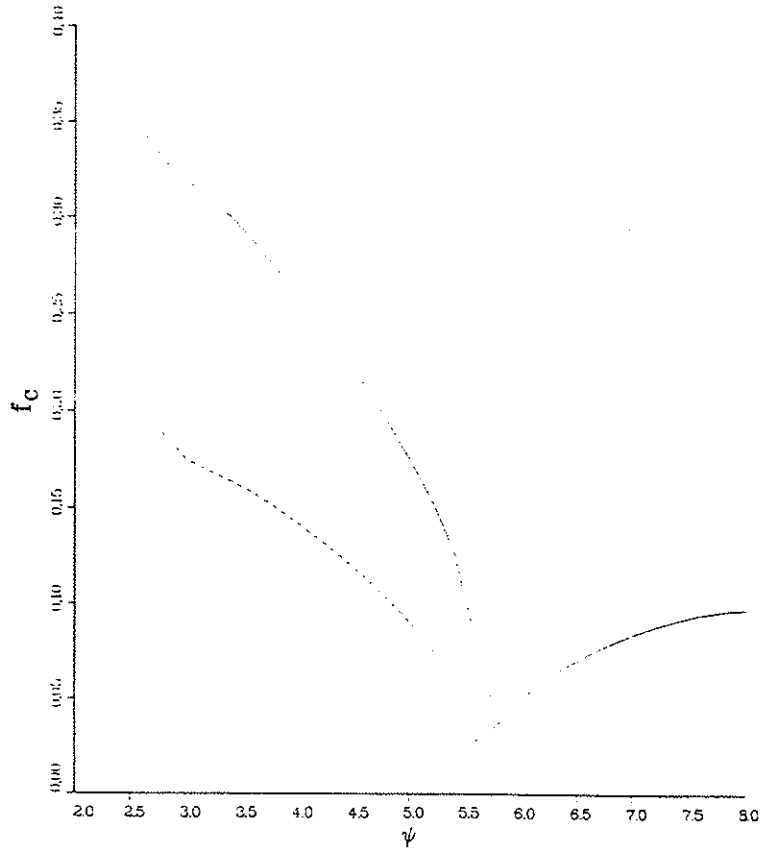

Fig. 3-6. Calculated $(1-\hat{L}_{31})$, from Eq. 3-37, versus λ_{ee}, the mean free path for $\psi = 6.5$. The solid curve is calculated using the fluid form for μ_{jk}^{ee} (Eq. 3-24), the dashed line uses the collisionless form (Eq. 3-31), and the dotted curve uses the smoothed coefficients (Eq. 3-41).

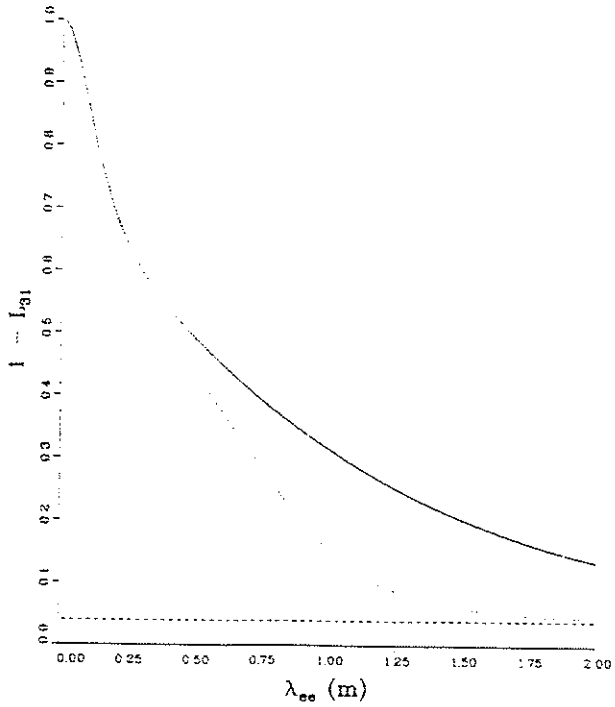

Fig. 3-7. Same as Fig. 3-6, but using Eq. 3-3 and thus ignoring the coupling to heat flow terms.

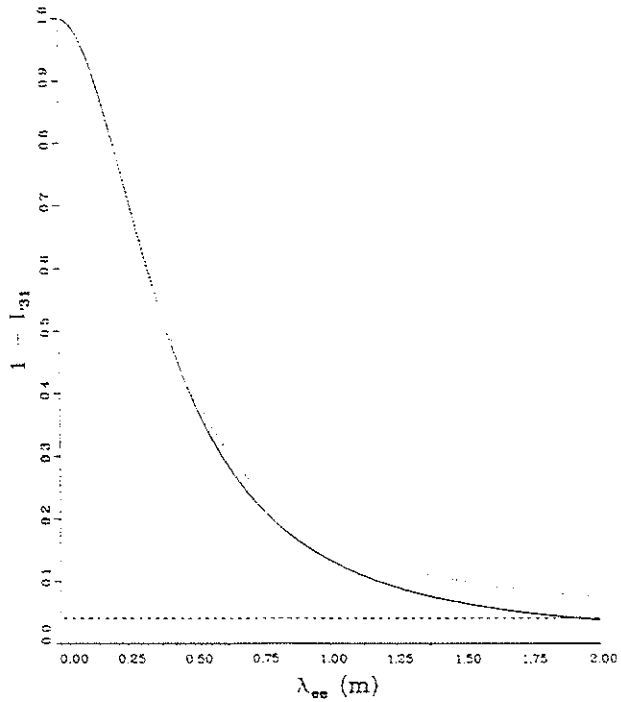

Fig. 3-8. Dependence of calculated $(1-\hat{L}_{31})$ on B_T for $\psi = 6.5$, $\lambda_{ee} = 0.5\,m$.

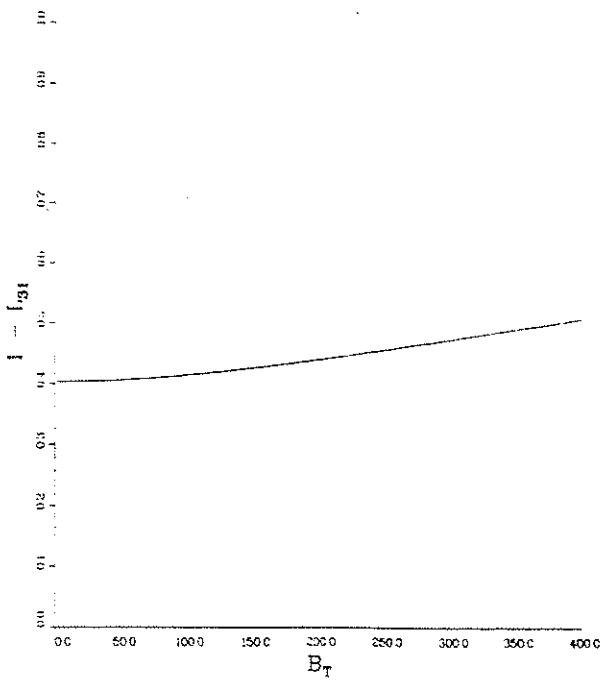

Fig. 3-9. Profile of calculated $(1 - \hat{L}_{31})$ for $\lambda_{ee} = 0.5\ m$.

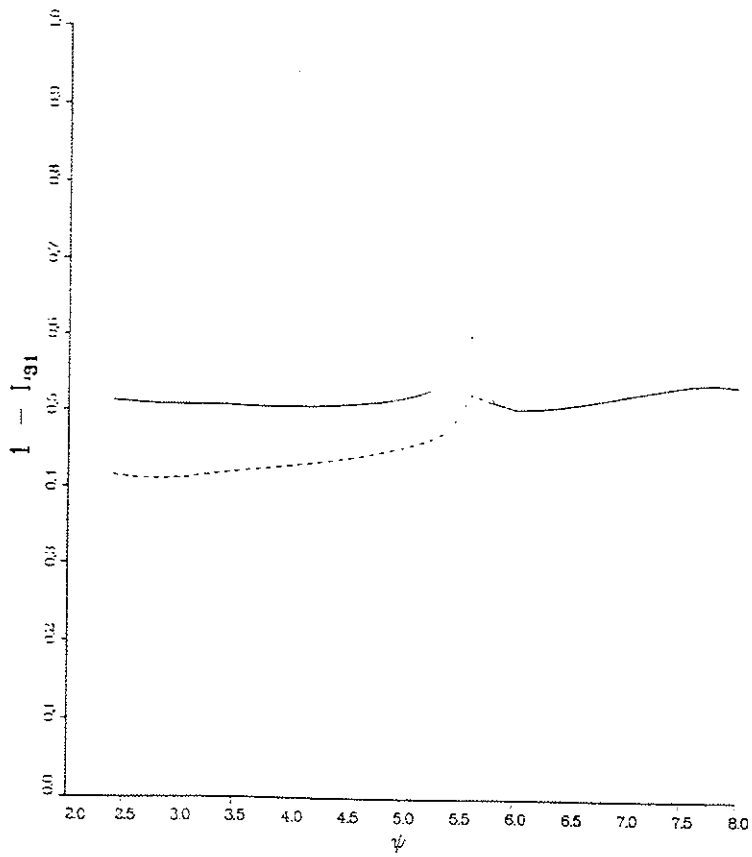

Fig. 3-10. Fraction of poloidal current carried by ions.

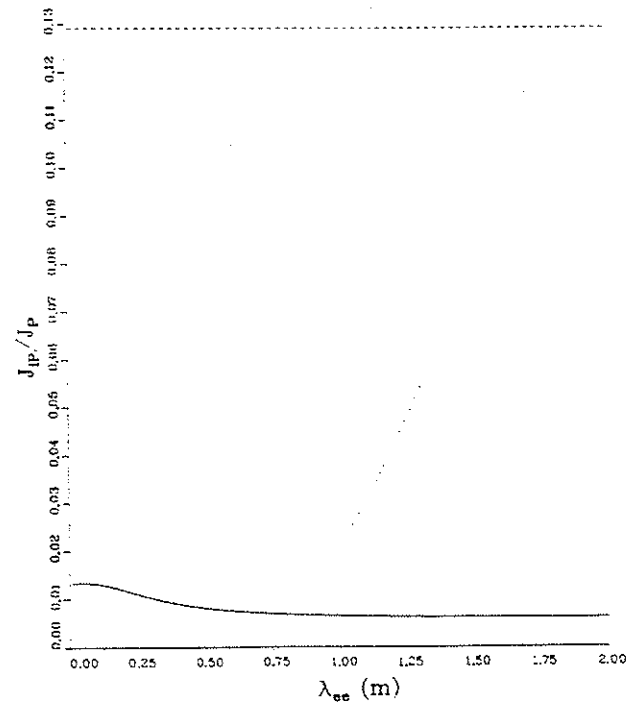

Fig. 3-11. Calculated $\hat{L}^{s}_{32}$ as a function of λ, for $B_T = 400\ G$ on axis. Different curves are for different forms of μ^{ss}_{jk}, as in Fig. 3-6.

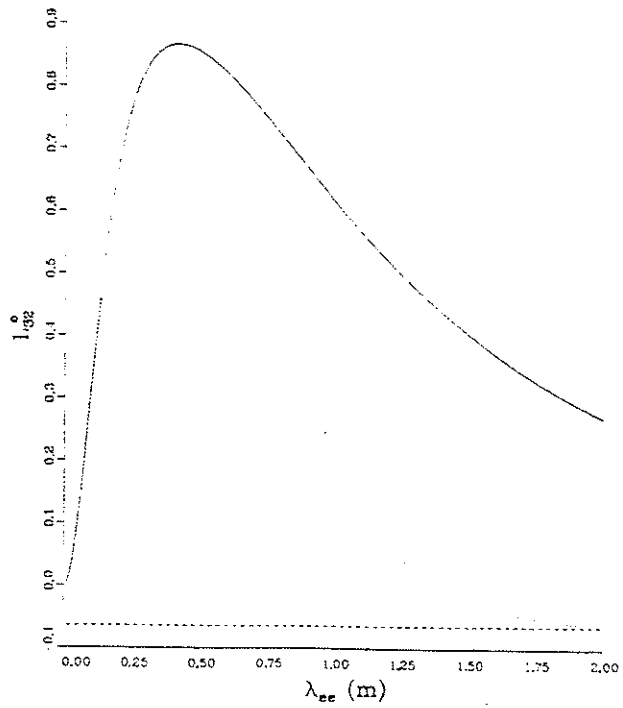

Fig. 3-12. Calculated $\hat{L}^{i}_{32}$ as a function of λ, for $B_T = 400\ G$ on axis. Different curves are for different forms of μ^{ee}_{jk}, as in Fig. 3-6.

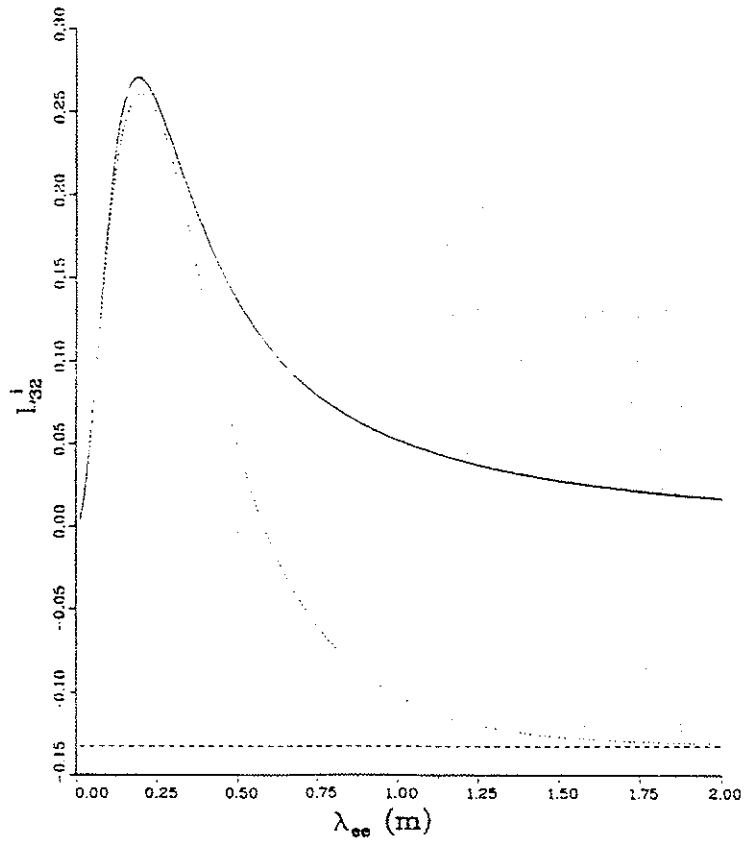

Chapter 4

Experimental Results

In this chapter the experimentally measured currents are discussed, and related to theoretical predictions. The total plasma current (ions and electrons) is discussed first, followed by the ion current.

4.1. Complete Current Measurements

Detailed measurements of the total current have been completed on several flux-surfaces, both inside and outside the separatrix. Data for the flux surfaces labeled (see section 2.1) $\psi = 4.5$, 6.5, and 7.0 are presented, showing the dependence of the plasma current on mean-free-path, poloidal angle, and B_T. It is seen that the measured currents generally agree with theoretical predictions, except for $\psi \geq 7.0$. All complete current data is taken using the magnetic probe technique described in section 2.3.2.

4.1.1. $\psi = 4.5$

The experimental and theoretical poloidal variation, within the $\psi = 4.5$ flux surface, of the complete perpendicular current component is shown in Fig. 4-1. This flux surface is just inside the separatrix. The perpendicular current is expected to vary as

$$j_\perp = R p' \frac{B_P}{B},$$

and the agreement with the experimental data further confirms the experimental technique (recall the comparison between the measured diamagnetic current profile and kinetic pressure profile in section 2.3.2.4). Fig. 4-2 shows the poloidal variation of the parallel current, taken at a time, during the discharge, when $\lambda_{ee} \simeq 2.0$ m and the plasma is in the banana regime. Also shown for comparison is the expected variation of the alternating sign Pfirsch-Schlüter term (the $\lim_{\lambda \to 0} j_\parallel$, when $\hat{L}_{31} \to 0$). Notice that most of the poloidal variation comes from the Pfirsch-Schlüter term (primarily the term necessary to maintain $\nabla \cdot \vec{j} = 0$), while the bootstrap current (difference between the experimental data and the Pfirsch-Schlüter curve) is uni-directional. The effective value of p' for scaling the theoretical curves was obtained by a least-squares-fit to the perpendicular current data points.

The collisionality dependence of the complete parallel current (normalized by p') is shown in Fig. 4-3 with the theoretical prediction. Also shown is the predicted value for the Pfirsch-Schlüter term. As expected, the measured parallel current approaches the Pfirsch-Schüter value as $\lambda_{ee} \to 0$. The difference between the experimental curve and the Pfirsch-Schüter value is a direct measure of the bootstrap current. The experimental curve is generated by observing the change in the currents while the plasma parameters decay (on a diffusive time scale) from 1.0 to 3.4 msec after injection.

The toroidal field dependence of the parallel current is shown in Fig. 4-4. The measured parallel current vanishes when $B_T = 0$, as expected for all neoclassical effects, and scales with B_T in agreement with theory.

Thus, the measured currents for $\psi = 4.5$ show quite good agreement with theory. Another flux surface inside the separatrix, $\psi = 4.0$, has also been investigated (but with fewer points in the poloidal scan) and is in similar good agreement with theory.

4.1.2. $\psi = 6.5$

The poloidal, collisionality, and B_T variations of the current for $\psi = 6.5$ are shown in Figs. 4-5, 4-6, 4-7 and 4-8. This flux surface is just outside the separatrix. The poloidal variation of the parallel and perpendicular components is in good agreement with theory. Again, the variation of the Pfirsch-Schlüter term is shown for comparison. The dependence on collisionality shows large non-reproducible fluctuations, but on the average is in agreement with theory, though there are large fluctuations. However, the toroidal field dependence is not in agreement with theory. For most B_T values, there is significantly more parallel current than expected, as there always is for $\psi = 7.0$, discussed below.

4.1.3. $\psi = 7.0$

The poloidal, collisionality, and B_T variations of the current for $\psi = 7.0$ are shown in Figs. 4-9, 4-10, 4-11 and 4-12. The poloidal variation of the perpendicular current, again, agrees well with theory. However,

while the variation of the parallel currents is reasonable, the *magnitude* of the parallel current does not agree with theory. Indeed, the disagreement indicates that too much boostrap current is flowing and $\hat{L}_{31} > 1$! Another way of viewing this is that the poloidal current has the wrong sign, since $j_P \propto (1 - \hat{L}_{31})$. The collisionality dependence (Fig. 4-11) shows that the parallel current evolves *away* from the Pfirsch-Schlüter value as $\lambda_{ee} \to 0$, in contrast to theoretical expectations, and the behaviour on the inner flux surfaces (e.g. Fig. 4-3). The B_T dependence (Fig. 4-12) of the poloidal current shows the correct scaling (proportional to B_T), even though the poloidal current is of opposite sign to the theoretically predicted value.

Thus, in contrast to the inner flux surfaces, for $\psi = 7.0$ the agreement between the measured parallel current magnitude and theory is not good, though the poloidal spatial variation and B_T scaling are correct. Less comprehensive measurements on other flux surfaces ($\psi = 7.5$ and 8.0) outside $\psi = 7.0$ show similar disagreements with theory, even though the perpendicular (diamagnetic) current always agrees with predictions (again see section 2.3.2.4).

While this disagreement is not presently understood, it is easily seen that it is *not* due to residual electric fields (from the time-changing vacuum magnetic fields) driving an Ohmic current. In the standard timing for the experiment, the peak magnetic field strength (and thus $\partial_t \vec{A} = 0$) occurs 1 msec after injection (see chapter 2). Fig. 4-13 shows the

time decay of the poloidal current density for three different shots, where injection occurs at (a) 3 msec early (4 msec before peak field), (b) standard time (1 msec before peak field), and (c) 3 msec late (2 msec after peak field). There is no significant difference between these cases, and certainly the poloidal current does not change sign. Thus any ohmic currents are experimentally insignificant, and cannot cause the observed disagreement with theory.

4.2. Ion Current Measurements

The ion portion of the current has been similarly studied, and found to be in good agreement with theory in all cases. The ion currents are measured using the double-sided Langmuir probe technique (see section 2.3.1). Fig. 4-14 shows the poloidal variation of the perpendicular component of the ion current for $\psi = 6.5$. The good agreement between the measured ion current and the predicted variation (Eq. 3-38) inspires confidence in the experimental method. The poloidal variation of the ion parallel current is shown in Fig. 4-15, for $\lambda \simeq 1.0$ m, in good agreement with theory. The experimental and theoretical collisionality dependence of the parallel ion current (normalized to p_i') is shown in Fig. 4-16. Note that $j_{\parallel i}$ and the Pfirsch-Schlüter term are of opposite sign at this location (the left-most point in Fig. 4-15), and that, in agreement with theory, $j_{\parallel i}$ does not approach the Pfirsch-Schlüter value as λ decays, in contrast to the total current. This is due to the ion viscosity coefficients always being much larger than the electron coefficients, independent of

collisionality. The poloidal variation of the components of the ion current, for $\psi = 7.0$ over a reduced poloidal range, is shown in Fig. 4-17. Again, both the perpendicular and parallel ion current show good agreement with theoretical predictions, even though the total parallel current on this flux surface is larger than expected (Fig. 4-11).

Thus, the ion current agrees well with theory. As such, since $T_i' \simeq 0$, this indicates the absence of poloidal ion flow, due to the higher ion viscosity (see section 3.3.3). In all cases, the measured ion current was consistent with no ion poloidal flow.

Fig. 4-2. Poloidal variation of parallel total current for $\psi = 4.5$, $\lambda \sim 1.5\ m$, theory (solid curve) and experiment (points). The dashed curve is the variation of the Pfirsch-Schlüter term ($\lambda \to 0$ limit of $j_\parallel$). The bootstrap current is the difference between the experimental data and the dashed curve.

Fig. 4-1. Poloidal variation of perpendicular (confining) current, for $\psi = 4.5$, theory (curve) and experiment (points).

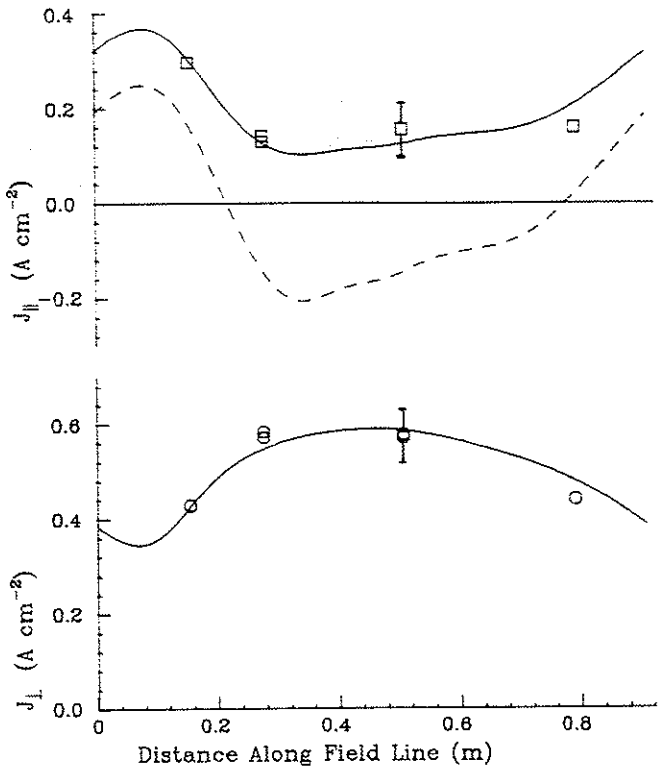

Fig. 4-3. Theoretical (dashed curve) and experimental collisionality dependence of complete parallel current, $\psi = 4.5$. Note that, at this location, the parallel current reverses sign in going from the collisionless to the collisional limits.

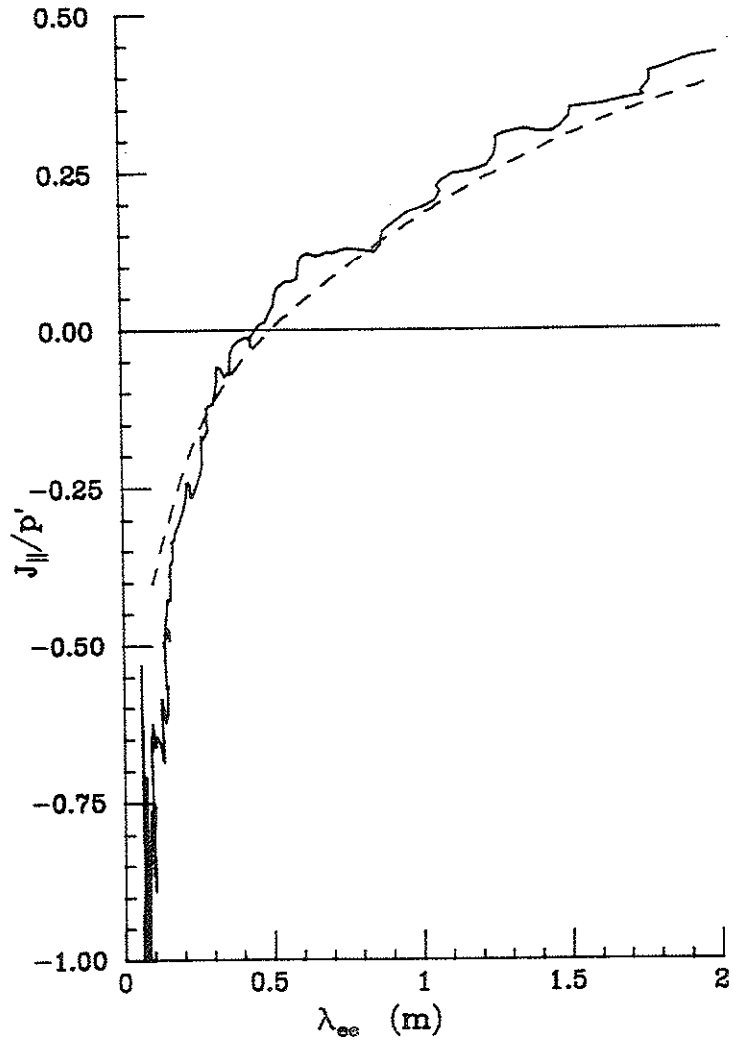

Fig. 4-4. Toroidal field dependence of complete poloidal current, experiment and theory, $\psi = 4.5$.

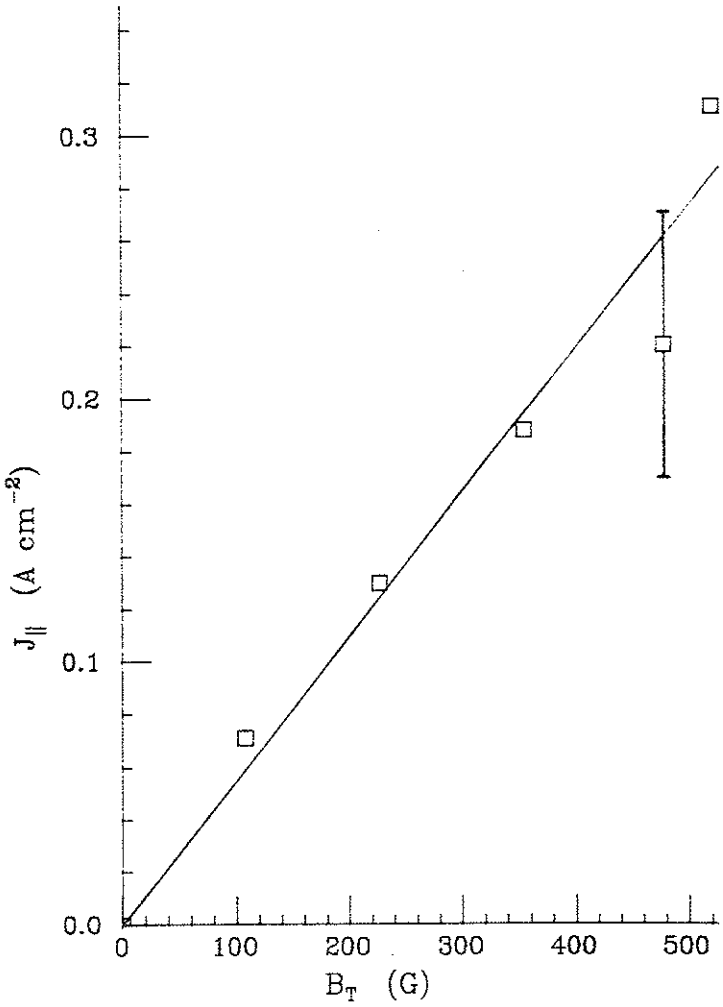

Fig. 4-6. Poloidal variation of parallel current, $\psi = 6.5$, for $B_T = 360$ G on axis. Curves are as in Fig. 3-2.

Fig. 4-5. Poloidal variation of perpendicular current, $\psi = 6.5$.

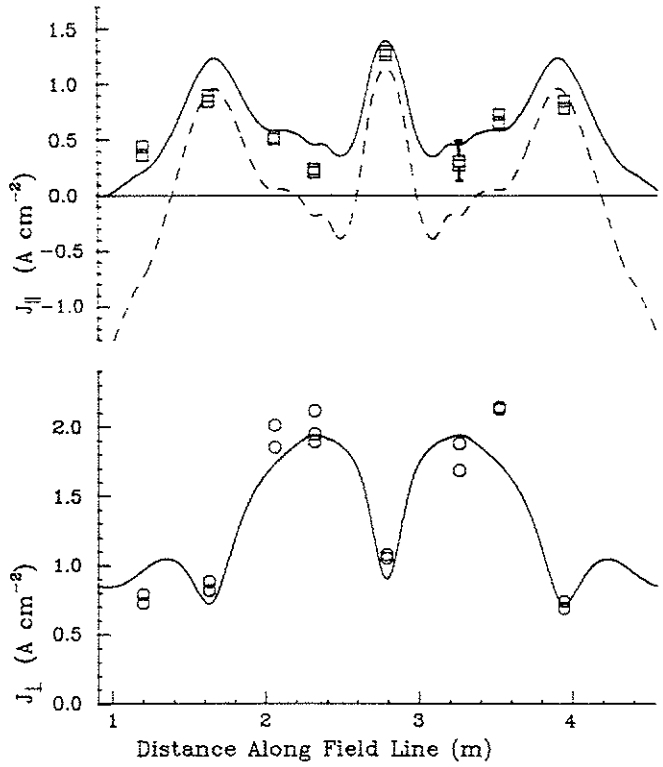

Fig. 4-7. Collisionality variation of parallel current for $\psi = 6.5$, $B_T = 360$ G. Note large fluctuations of measured current from expected values.

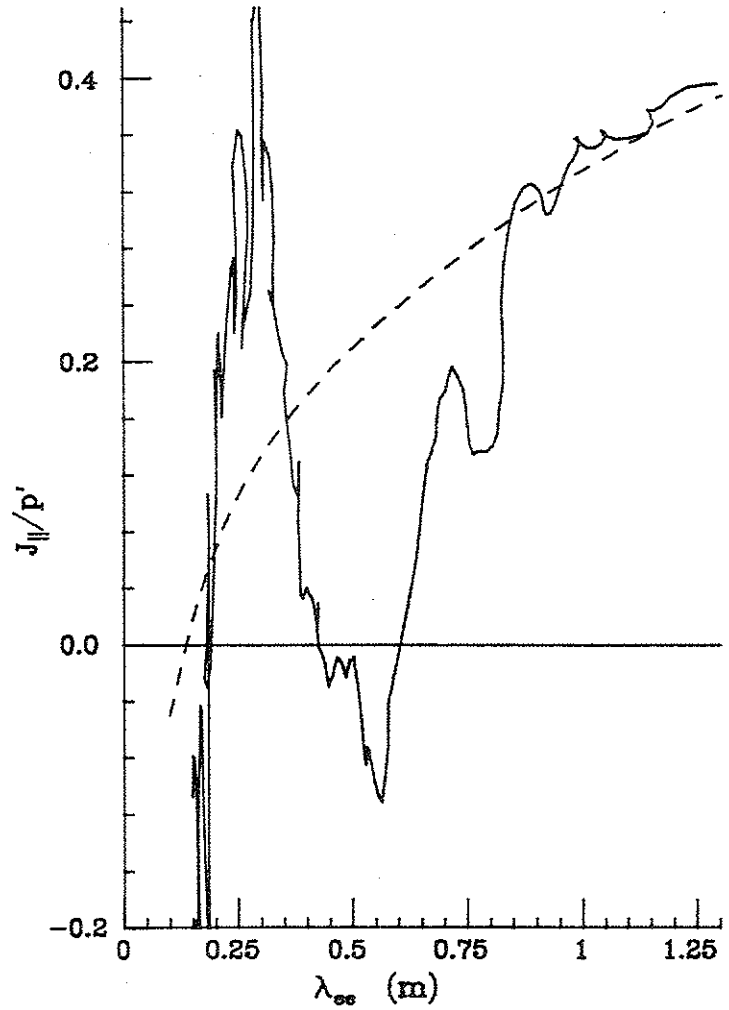

Fig. 4-8. Toroidal field dependence of complete poloidal current, experiment and theory. $\psi = 6.5$. Note that, except for a region near $B_T = 350 - 400$ G, there is more parallel current than expected.

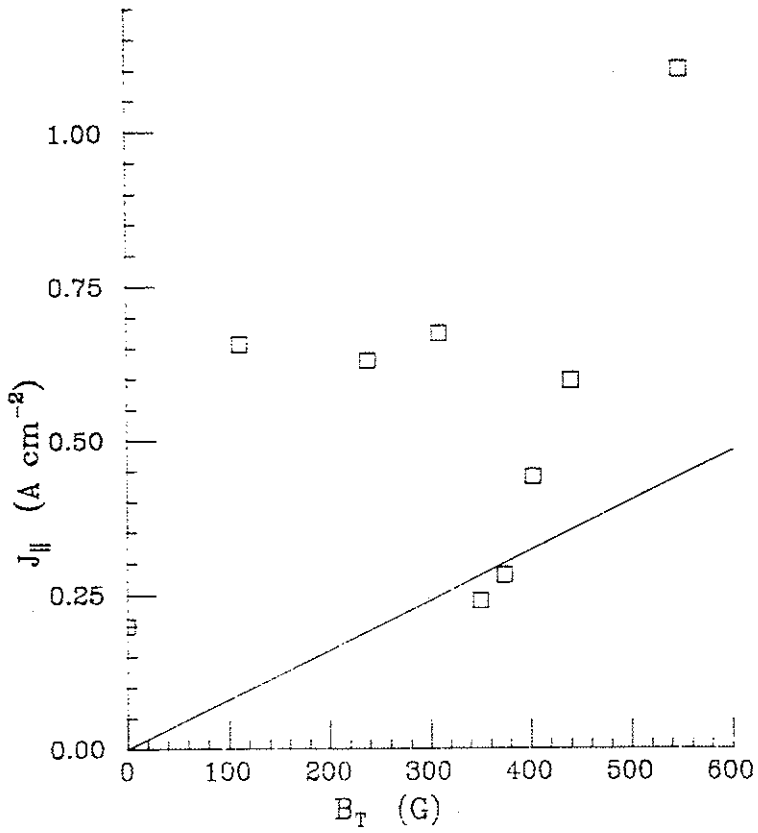

Fig. 4-10. Poloidal dependence of $j_{\parallel}$ for $\psi = 7.0$, $B_T = 400$ G on axis.

Fig. 4-9. Poloidal variation of $j_{\perp}$ for $\psi = 7.0$.

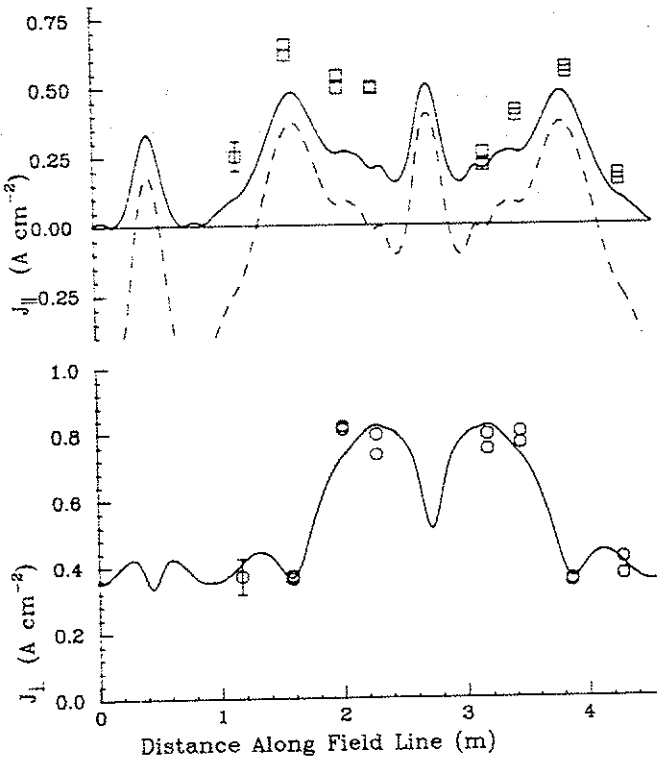

Fig. 4-11. Collisionality dependence of $j_{\parallel}$ for $\psi = 7.0$, $B_T = 400\ G$ on axis. Note excess of parallel current, and that the excess grows as $\lambda \to 0$.

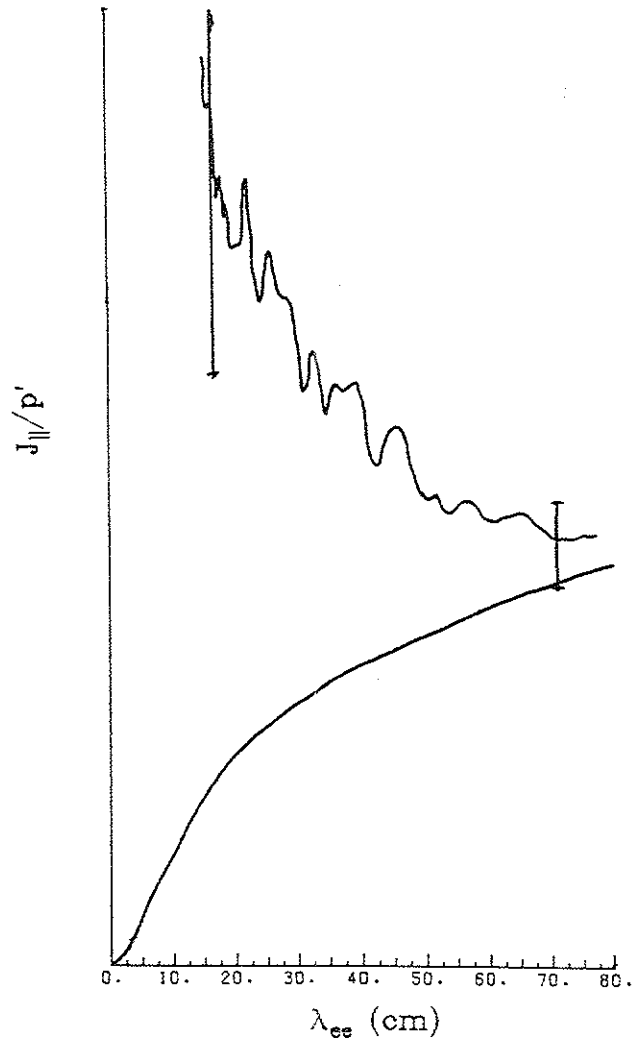

Fig. 4-12. B_T dependence of poloidal current. The solid curve does not denote the theoretically predicted value, but the expected (linear) variation of the current. Even though there is too much parallel current (and the poloidal current has the wrong sign) it has the correct variation with B_T.

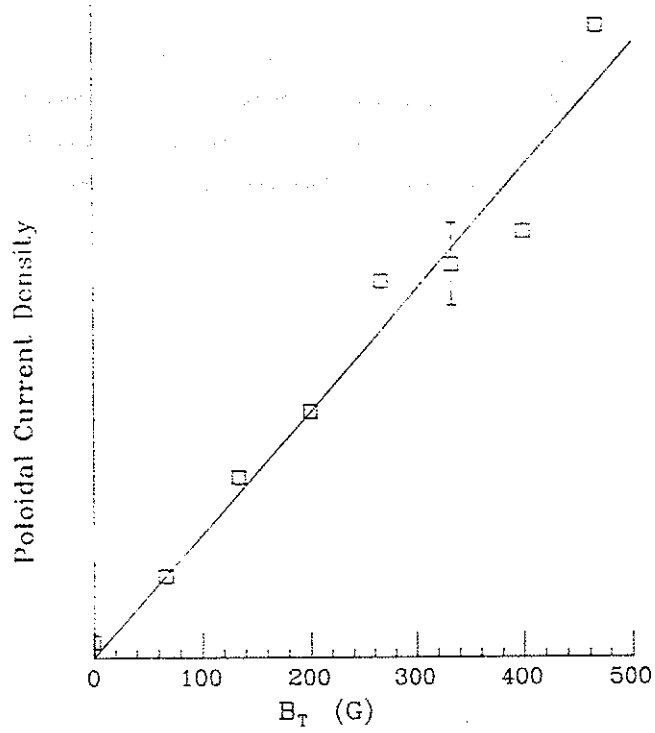

Fig 4-13. Time decay of poloidal current after injection, $\psi = 7.0$, for different injection times (after the start of the inductive vacuum field puise). showing that any inductive electric fields are not responsible for the problems on $\psi = 7.0$. Peak field occurs at 20.1 msec.

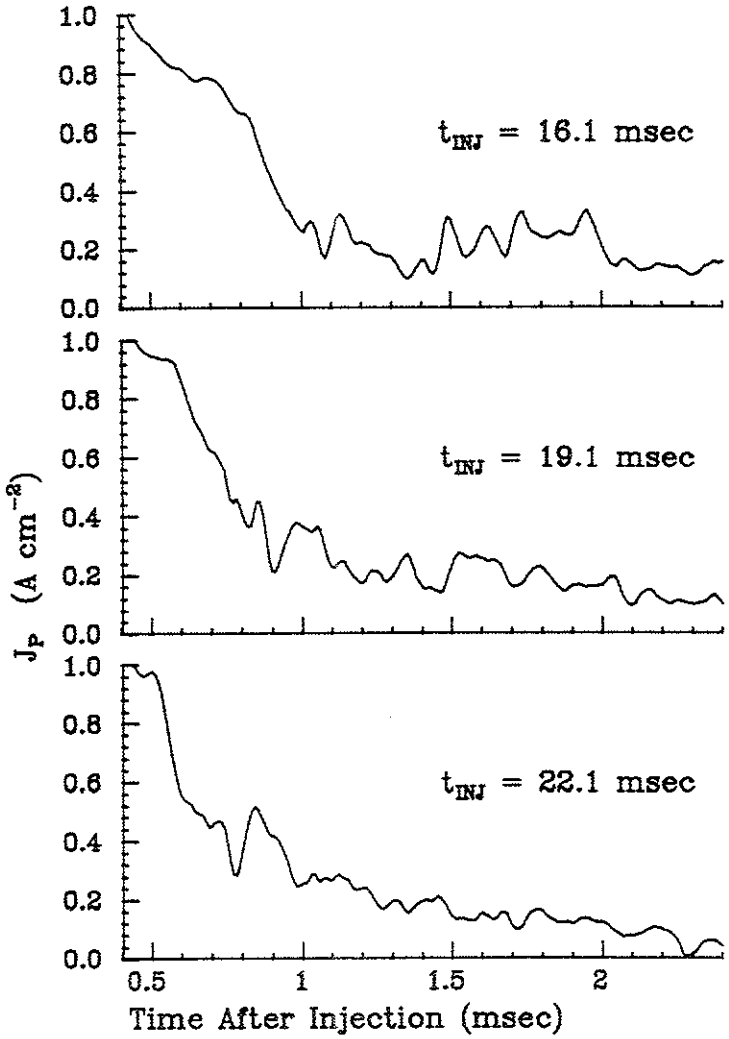

Fig. 4-15. Poloidal variation of the ion parallel current, for $\psi = 6.5$ and $B_T = 400\,G$ on axis.

Fig. 4-14. Poloidal variation of ion perpendicular current, for $\psi = 6.5$.

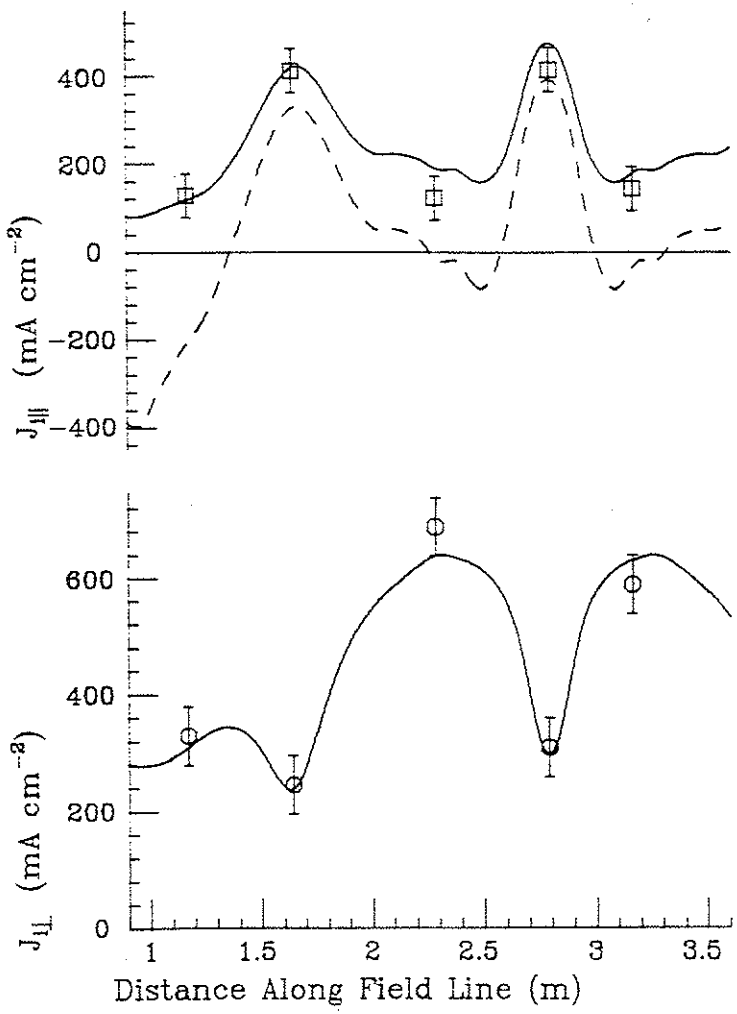

Fig. 4-16. Collisionallity dependence of ion parallel current, $\psi = 6.5$. Note that, as expected, the ion parallel current does not approach the Pfirsch-Schlüter value as $\lambda \to 0$, due to the high ion viscosity.

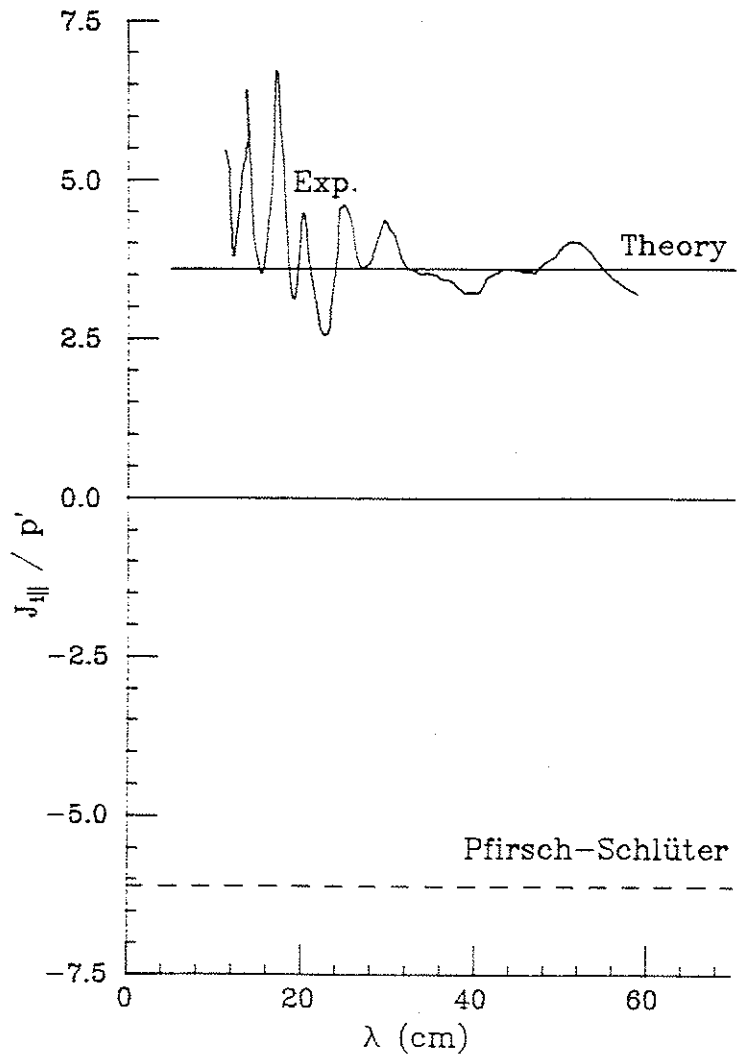

Fig. 4-17. Poloidal variation of ion parallel and perpendicular currents for $\psi = 7.0$.

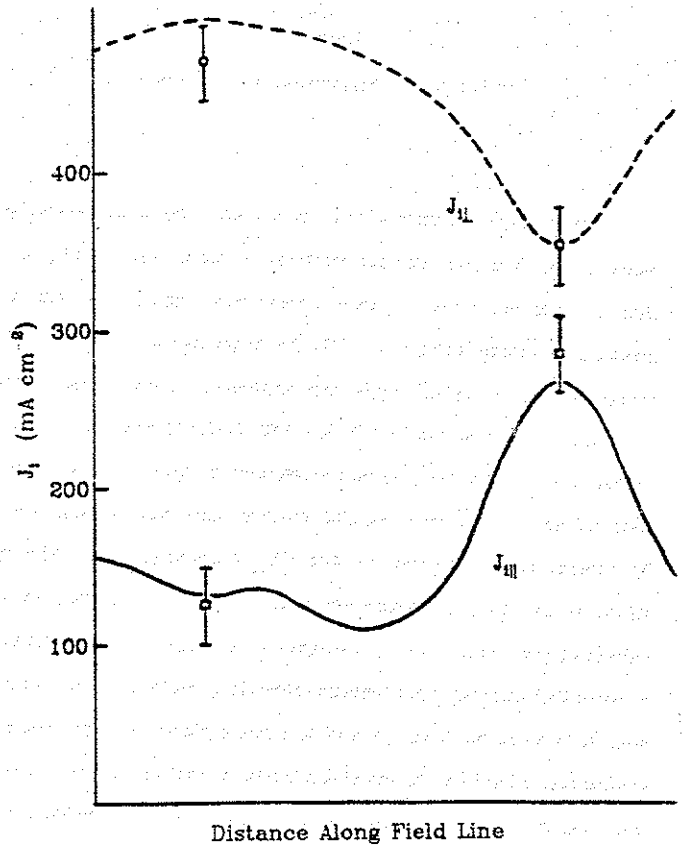

Chapter 5

Conclusion and Suggestions for Further Work

Detailed measurements of the collisionality, B_T, and poloidal dependence of both the total and ion currents in the Levitated Octupole show that: (1) The ion current always agrees with theory, the ions do not measurably rotate poloidally. (2) The total current agrees well with theory on flux surfaces inside the separatrix, showing the bootstrap current and decaying (as $\lambda \to 0$) to the Pfirsch-Schlüter limit, as expected. (3) For flux surfaces far outside the separatrix, agreement with theory is poor, in that there is more parallel current than expected and the parallel current does not decay to the Pfirsch-Schlüter limit. The spatial structure and B_T dependence are otherwise correct, showing variations indicating that the current is divergence-free. The extra parallel current is not ohmic current from residual electric fields due to the inductively generated magnetic field. (4) ψ=6.5, a flux surfaces near but outside the separatrix, resembles the inner flux surfaces and agrees with theory for some values of B_T. For other values of B_T, ψ=6.5 resembles the outer flux surfaces, and has too much parallel current.

These measurements strongly support the basic validity of neoclassical transport theory, and demonstrate that the bootstrap and Pfirsch-

Schlüter currents do indeed exist at current levels of the order of 1 A/cm^2. The inability of other experiments to detect these currents may be related to the cause of the lack of agreement between theory and experiment on the outer flux surfaces, or may be due other effects avoided in this experiment such as Ohmic current.

A clear area for further investigation is the lack of agreement between theory and measured total parallel current on the outer flux surfaces. A tantalizing speculation is that the lack of agreement is due to the enhanced fluctuation levels in the outer (average good curvature) surfaces.[34] Experimentally measured diffusion coefficients (with no B_T) are consistent with classical diffusion on flux surfaces inside the separatrix but greatly exceed classical outside.[34] It will be important to ensure that residual field errors on the outside of the device (say, due to additional imperfections in the vacuum vessel) are not causing these problems.

There is continuing effort by the group to study any effect on these currents due to a variety of phenomena present on other magnetic confinement devices, in particular: (1) fluctuations, inherent or induced; (2) Ohmic current; and (3) ion cyclotron heating.

References

1. A.A. Galeev and R.Z. Sagdeev, *Zh. Eksp. Teor. Fiz.* **53**, 348 (1967)[*Sov. Phys.-JETP* **26**, 233 (1968)]
2. F.L. Hinton and R.D. Hazeltine, *Rev. Mod. Phys.* **48**, 239 (1978)
3. S.I. Braginskii, in *Reviews of Plasma Physics, Vol. I*, ed. M.A. Leontovich, Consultants Bureau, New York (1965) 205
4. A.A. Galeev, *Zh. Eksp. Teor. Fiz.* **59**, 1378 (1970)[*Sov. Phys.-JETP* **32**, 752 (1971)]
5. R.J. Bickerton, J.W. Conner, and J.B. Taylor, *Nat. Phys. Sci.* **229**, 110 (1971)
6. L.D. Pearlstein, T.B. Kaiser, and W.A. Newcomb, *Phys. Fluids* **24**, 1326 (1981)
7. D. Pfirsch and A. Schlüter, Report MPI/PA/7/62, Max Planck Institute (1962).
8. C. Bolton and A.A. Ware, *Phys. Fluids* **26**, 459 (1983)
9. M.S. Berezhetsky, S.E. Grebentshikov, I.A. Kossy, I.S. Sbitnikova, and I.C. Shpigel, in *Plasma Physics and Controlled Nuclear Fusion Research, Vol. III*, IAEA, Vienna (1971) 49
10. R.A.E. Bolton, J. Hugill, D.J. Lees, W. Millar, and P. Reynolds, in *Plasma Physics and Controlled Nuclear Fusion Research, Vol. III*, IAEA, Vienna (1971) 79

11. A.G. Dikii, Yu.K. Kuznetsov, V.K. Pashnev, and V.M. Tonkopryad, *Fiz. Plazmy* **3**, 6 (1977)[*Sov. J. Plasma Phys.* **3**, 2 (1977)]
12. J.T. Hogan, *Nucl. Fusion* **21**, 365 (1981)
13. J.H. Halle, A.G. Kellman, R.S. Post, S.C. Prager, E.J. Strait, and M.C. Zarnstorff, *Phys. Rev. Lett.* **46**, 1394 (1981)
14. A.G. Kellman, M.W. Phillips, S.C. Prager, and M.C. Zarnstorff, *Nucl. Fusion* **23**, 1561 (1983)
15. S.P. Hirshman and D.J. Sigmar, *Nucl. Fusion* **21**, 1079 (1981)
16. D.W. Kerst and et al., in *Plasma Physics and Controlled Nuclear Fusion Research, Vol. I*, IAEA, Vienna (1971) 3
17. J.D. Steben, *J. Appl. Phys.* **43**, 1211 (1972)
18. J.R. Drake, Ph.D. Thesis, Nucl. Engr. Dept., University of Wisconsin, Madison, Wi. (1974).
19. A.J. Cavallo, Ph.D. Thesis, Physics Dept., University of Wisconsin, Madison, Wi. (1975).
20. C.J. Armentrout, Ph.D. Thesis, Physics Dept., University of Wisconsin, Madison, Wi. (1977).
21. R.L. Willig, Report PLP 471, Physics Dept., University of Wisconsin, Madison, Wi. (1972).
22. D.C. Morin, Report PLP 523, Physics Dept., University of Wisconsin, Madison, Wi. (1973).

23. H.R. Garner, Report PLP 833, Physics Dept., University of Wisconsin, Madison, Wi. (1980).

24. F.F. Chen, in *Plasma Diagnostic Techniques*, ed. R.H. Huddlestone and S.L. Leonard, Academic, New York (1965) 113

25. J.C. Sprott, *Rev. Sci. Instr.* **39**, 1569 (1968)

26. T.L. Owens, Ph.D. Thesis, Elect. Engr. Dept., University of Wisconsin, Madison, Wi. (1979).

27. P. Nonn, private communication

28. D.A. Brouchous, Ph.D. Thesis, Physics Dept., University of Wisconsin, Madison, Wi. (1980).

29. D. Lencioni, Report PLP 205, Physics Dept., University of Wisconsin, Madison, Wi. (1968).

30. Sauereisen Cements Co., Pittsburgh, Penn.

31. Precision Monolithics, Inc., Santa Clara, Ca.

32. Intersil, Inc., Cupertino, Ca.

33. H.R. Garner, Ph.D. Thesis, Nucl. Engr. Dept., University of Wisconsin, Madison, Wi. (1982).

34. A.G. Kellman, Ph.D. Thesis, Physics Dept., University of Wisconsin, Madison, Wi. (1983).

35. L. Spitzer, Jr., *Physics of Fully Ionized Gases*, Interscience, New York (1962).

36. F.L. Hinton and C. Oberman, *Nucl. Fusion* **9**, 319 (1969)

37. S.I. Braginskii, *Zh. Eksp. Teor. Fiz.* **33**, 459 (1957)[*Sov. Phys. JETP* **6**, 358 (1958)]

38. R.D. Hazeltine, *Plasma Phys.* **15**, 77 (1973)

39. P.H. Rutherford, *Phys. Fluids* **13**, 482 (1970)

40. M. Abramowitz and I.A. Stegun, *Handbook of Mathematical Functions*, National Bureau of Standards, USGPO, Washington, D.C. (1964).

41. S.P. Hirshman and D.J. Sigmar, *Phys. Fluids* **19**, 1532 (1976)

42. G.F. Chew, M.L. Goldberger, and F.E. Low, *Proc. R. Soc. London* **236**, 112 (1956)

43. S.P. Hirshman and A.H. Boozer, PPPL-1409, Princeton Plasma Physics Laboratory, Princeton, NJ (Dec. 1976).

44. A.H. Boozer, Report EPRI-4, Princeton Plasma Physics Laboratory, Princeton, NJ (1976).

45. R.C. Grimm and J.L. Johnson, *Plasma Phys.* **14**, 617 (1972)

46. K.C. Shaing and J.D. Callen, *Phys. Fluids* **26**, 1526 (1983)

47. H.K. Meier, S.P. Hirshman, D.J. Sigmar, and L.L. Lao, ORNL/TM-7584, Oak Ridge National Laboratory, Oak Ridge, Tn. (March 1981).

48. S.P. Hirshman and D.J. Sigmar, *Phys. Fluids* **20**, 418 (1977)

49. S.P. Hirshman, D.J. Sigmar, and J.F. Clarke, *Phys. Fluids* **19**, 656 (1976)